The encoding of touch by somatotopically aligned dorsal column subdivisions

Josef Turecek, Brendan P. Lehnert, and David D. Ginty

Department of Neurobiology, Howard Hughes Medical Institute, Harvard Medical School,
220 Longwood Avenue, Boston, MA 02115

Correspondence: david_ginty@hms.harvard.edu

ABSTRACT

The somatosensory system decodes a range of tactile stimuli to generate a coherent sense of touch. Discriminative touch of the body depends on signals conveyed from peripheral mechanoreceptors to the brain via the spinal cord dorsal column and its brainstem target the dorsal column nuclei (DCN)[1,2]. Models of somatosensation emphasize that fast-conducting low-threshold mechanoreceptors (LTMRs) innervating the skin drive the DCN[3,4]. However, post-synaptic dorsal column neurons (PSDCs) within the spinal cord dorsal horn also collect mechanoreceptor signals and form a second major input to the DCN[5–7]. The significance of PSDCs and their contributions to the coding of touch have remained unclear since their discovery. Here, we show that direct LTMR inputs to the DCN convey vibrotactile stimuli with high temporal precision, whereas PSDCs primarily encode touch onset and the intensity of sustained contact into the high force range. LTMR and PSDC signals topographically re-align in the DCN to preserve precise spatial detail. Different DCN neuron subtypes have specialized responses that are generated by unique combinations of LTMR and PSDC inputs. Thus, signals encoding different tactile features are conveyed by subdivisions of the dorsal column pathway and differentially converge in the DCN to generate unique ascending signals suited to distinct sensory processing streams.

MAIN TEXT

Fast-conducting low-threshold mechanoreceptors (Aβ-LTMRs) detect light mechanical forces acting on the skin and mediate discriminative touch[8–11]. Aβ-LTMR signals are conveyed rapidly from the periphery, and their axons ascend the dorsal column of the spinal cord and directly contact the dorsal column nuclei (DCN) of the brainstem. From the DCN, mechanosensory information is relayed to multiple targets in higher brain regions. Sensory information is conveyed from the DCN to the somatosensory cortex via a prominent projection to the somatosensory ventral posterolateral thalamus (VPL) for the conscious perception of touch. A separate, lesser-known population of DCN neurons relays tactile information to the external cortex of the inferior colliculus (IC)[12,13] where it is integrated and contextualized with auditory information. Other populations of DCN neurons project to the olivocerebellar system[14,15] to coordinate motor adaptation, and to secondary thalamic nuclei[16] involved in affective state. Thus, the DCN is a conduit of incoming mechanosensory signals, broadly connecting mechanoreceptors in the periphery to several major brain areas.

Somatosensory coding in DCN neurons is known to be heterogeneous[17–20], but how tactile signals are organized within the DCN and distributed to downstream targets remains unknown. Thus, we selectively recorded from DCN (gracile nucleus, **Extended Data Fig. 1**) neuron subtypes of the mouse using antidromic activation and optogenetic tagging to determine how sensory representations of the hindlimb are encoded at this early stage of the somatosensory hierarchy.

We found that different DCN neuron types encode distinct aspects of mechanosensory stimuli suited to their projection targets. DCN neurons projecting to the VPL (VPL-PNs) are the most abundant cell type in the DCN, outnumbering inferior colliculus projection neurons (IC-PNs) and local inhibitory interneurons (Vgat-INs) with an estimated proportion of VPL-PN:IC-PN:Vgat-IN of 2:1:1 (ref.[13]). We found that VPL-PNs had small excitatory receptive fields with large regions of surround suppression (**Fig. 1A-C, P-Q, Extended Data Table 1-2**). These VPL-PNs could entrain their firing to mechanical vibration, but for the vast majority this entrainment was restricted to a narrow range of frequencies below 150 Hz (**Fig. 1C-D**). DCN neurons projecting to the IC could be classified into several sub-groups (**Extended Data Fig. 2**), but most commonly had very large and exclusively excitatory receptive fields that included the entire hindlimb (**Fig. 1F-H, P**). Unlike VPL-PNs, most IC-PNs could entrain their firing to mechanical

vibration across a broad range of frequencies (**Fig. 1H-I**). Vibration of the hindlimb evoked precisely timed action potentials that were entrained and phase-locked to vibrations ranging from 10 Hz up to 500 Hz, the highest frequency tested. Thus, neurons projecting to the VPL are tuned to convey finely detailed spatial information, whereas neurons projecting to the IC poorly encode spatial detail and are better suited to encode a broad range of mechanical vibrations that may be correlated with auditory stimuli. Inhibitory interneurons had a wide range of receptive field sizes, lacked inhibitory surrounds, and unlike PNs typically lacked spontaneous firing (**Fig. 1K-N, P, R**). All three DCN cell types rapidly adapted to step indentations at low forces (**Fig. 1E, J, O**). In contrast to other cell types, VPL-PNs could more reliably encode the static phase of sustained high force indentation, well above forces at which Aβ-RA-LTMRs and Aβ-SA-LTMRs plateau (**Fig. 1E**)[21–24].

We next addressed how the unique response properties of VPL-PNs and IC-PNs are generated. Aβ-LTMR axons that travel via the dorsal column form the 'direct' dorsal column pathway from the skin to the DCN and synapse directly upon DCN PNs and interneurons. However, post-synaptic dorsal column neurons (PSDCs) of the spinal cord, which receive input from a broad array of somatosensory neuron subtypes, including Aβ-LTMRs, also project to the DCN via an 'indirect' dorsal column pathway that exists across mammals, including primates[25–33]. PSDCs form up to 40% of the axons ascending the dorsal column (**Extended Data Fig. 3**)[34], but the function of PSDCs and their contribution to somatosensory representations in the DCN and higher brain regions have remained unclear since their discovery. We hypothesized that direct and indirect dorsal column pathway projections contribute uniquely to the distinct tuning features of DCN neuron subtypes.

In order to isolate the functions of direct and indirect dorsal column inputs to DCN neuron responses, we used the light-activated chloride channel Acr[35] to reversibly silence axon terminals of ascending inputs. We first generated *Cdx2-Cre; Rosa26*$^{LSL\text{-}Acr1}$ mice to express Acr1 in all neurons below the neck to reversibly silence both primary sensory (direct pathway) and PSDC (indirect pathway) neurons that provide input to the DCN (**Fig. 2A; see methods**). We transiently silenced axon terminals in the DCN by preceding mechanical stimuli with brief, 300-400 ms light ramps (**Extended Data Fig. 4**), which was optimal for suppressing excitatory inputs (**see Methods**). Mechanical stimuli were delivered in the final 100-200 ms of light application.

86 Using this strategy to silence both the direct and indirect dorsal column pathway inputs abolished
87 almost all DCN responses to vibration and low force step indentation of the hindlimb (**Fig. 2 B-**
88 **E**). We next selectively silenced all direct dorsal column pathway (Aβ-LTMR) input using
89 *Avil*^{Cre}*; Rosa26*$^{LSL\text{-}Acr1}$ mice, allowing us to determine how the indirect pathway contributes to
90 responses in individual DCN neurons (**Fig. 2F**). When light ramps were applied to silence Aβ-
91 LTMR axon terminals in the DCN to block direct pathway inputs, the amplitude of responses
92 were reduced but not eliminated. Thus, the indirect pathway was able to convey signals from
93 low-frequency (10 Hz) mechanical stimuli to generate responses in the DCN (**Fig. 2G-H**).
94 Silencing LTMR input also affected the response to step indentations, but the indirect pathway
95 was able to reliably convey the onset and, in most units, the offset of low-threshold step
96 indentation stimuli (**Fig. 2I-J**). On the other hand, indirect pathway input failed to evoke firing in
97 response to 50 Hz and 300 Hz vibratory stimuli. Thus, high-frequency time-varying light touch
98 stimuli such as vibration are exclusively encoded by the direct dorsal column pathway, whereas
99 both the direct and indirect dorsal column pathway contribute to responses to gentle or light skin
100 displacement.

101 VPL-PNs can encode spatial information in part due to their prominent inhibitory surround
102 receptive fields, and we therefore asked how the direct and indirect dorsal column pathways
103 contribute to surround inhibition of these PNs (**Fig. 2K**). Spontaneously active VPL-PNs can be
104 most effectively inhibited by applying brief vibratory stimuli to areas outside of their excitatory
105 receptive field. Surround suppression is often followed by rebound firing upon release from
106 inhibition (**Fig. 2L, M**). Silencing Aβ-LTMR axon terminals in the DCN almost completely
107 abolished inhibitory surround and rebound firing (**Fig. 2L-Q**), suggesting that the direct dorsal
108 column pathway is the primary driver of inhibitory surround receptive fields in VPL-PNs.

109 We next asked how PSDCs and the indirect pathway may contribute to DCN representations of
110 other features of mechanical stimuli. As no genetic tools currently exist to selectively silence
111 PSDCs, we used a pharmacological approach to block the indirect dorsal column pathway (**Fig.**
112 **3A**). Excitatory synaptic transmission in the lumbar spinal cord dorsal horn can be effectively
113 blocked by application of glutamate receptor antagonists directly to the dorsal surface of the
114 lumbar cord (**Extended Data Fig. 5**), thereby eliminating hindlimb-level PSDC neuron
115 activation and contributions to responses recorded in the DCN. This glutamatergic transmission

116 blockade was spatially restricted to the spinal cord region to which it was applied, since
117 glutamate receptor antagonists applied to the lower thoracic cord did not affect DCN responses
118 to mechanical stimulation of the hindlimb (**Extended Data Fig. 6**). When fast excitatory
119 transmission was blocked in the lumbar spinal cord, DCN neurons could still entrain and phase-
120 lock their spiking to a broad range of vibration frequencies of mechanical stimuli applied to the
121 hindlimb (**Fig. 3B, C**). This finding, which is consistent with the Acr1 silencing experiments
122 (**Fig. 2H**), indicates that Aβ-LTMR input via the direct dorsal column pathway underlies high-
123 frequency vibration tuning in the DCN.

124 Another salient feature encoded by DCN neurons is stimulus intensity. We applied step
125 indentations to the skin using blunt and smoothed probes (1-mm diameter) that did not damage
126 the skin even at high forces, but generated graded, compressive stimuli from the low to high
127 force range (1-300 mN). We found that under normal conditions DCN neurons were extremely
128 sensitive to the onset and offset of low-force indentations, as expected, but also fired in response
129 to sustained indentation of the skin, especially at high forces (**Fig. 3D-F**). Sustained firing during
130 maintained step indentations was proportional to the force applied. DCN neurons could therefore
131 not only detect the onset and offset of very gentle stimuli, but could also encode sustained
132 mechanical stimuli across a broad range of intensities, into the high force range (**Fig. 3F**).

133 When excitatory transmission was blocked in the spinal cord to suppress PSDC input, firing
134 during the sustained phase of indentation was almost eliminated across all forces for most DCN
135 neurons (**Fig. 3G-K**). Thus, in the absence of PSDC input, DCN neurons could no longer encode
136 the intensity of maintained stimuli (**Fig. 3M**). We also found that attenuating PSDC input to the
137 DCN raised the threshold of DCN neurons to the onset of step indentation (**Fig. 3L**). These
138 findings suggest that PSDCs provide graded force information to the DCN, enabling responses to
139 sustained high intensity stimuli. At the same time, PSDCs also contribute to detection of gentle
140 touch stimuli. Thus, PSDCs and the indirect dorsal column pathway are required for the wide
141 dynamic range of intensity tuning in DCN neurons, enabling detection and encoding of a broad
142 range of stimulus intensities. We also found that the graded coding of intense stimuli in the DCN
143 was relayed upstream to middle VPL (mVPL) neurons, and that both low-threshold sensitivity
144 and sustained responses to high-threshold stimuli in the mVPL were strongly dependent on the
145 DCN (**Extended Data Fig. 7**). Moreover, although many neurons in the DCN are spontaneously

active, we found that eliminating dorsal column input to the DCN did not have major effects on spontaneous firing, suggesting that PSDCs do not drive spontaneous firing in the DCN (**Extended Data Fig. 8**).

The observation that DCN neurons encode high intensity indentation stimuli is noteworthy because most Aβ-LTMRs are thought to saturate their firing at relatively low indentation forces[21–24]. As most of the high force responses of DCN neurons during sustained indentations are mediated by PSDC neurons, we considered the possibility that PSDCs transmit signals emanating from both LTMRs and high-threshold mechanoreceptors (HTMRs), which do not project directly to the DCN via the direct dorsal column pathway[36]. In order to activate HTMRs without concurrent activation of LTMRs, we expressed the light-activated cation channel ReaChR in somatosensory neurons expressing *Calca* (CGRP) using *Calca-FlpE*; *Rosa26*$^{FSF\text{-}ReaChR}$ mice[37,38] and applied light directly to the skin of the hindlimb (**Fig. 4A**). Among sensory neurons expressing *Calca* are A-fiber HTMRs as well as a subset of C-fiber HTMRs[39–42]. As before, VPL-PNs responded rapidly to strong mechanical step indentations of the skin with additional long latency spikes (**Fig. 4B**). Optical excitation of Calca^{+} HTMRs within the same area of skin triggered firing in VPL-PNs with fast latencies that were consistent with A-fiber activation, but were longer than those evoked by mechanical stimuli (**Fig. 4C, D**). These rapid optogenetically-evoked responses were sometimes followed by a second and much longer latency burst (**Fig. 4E-G**). These two temporal components of firing were consistent with the activation of intermediate and slow conducting Aδ and C fiber neurons known to express *Calca*[40]. Strikingly, almost all VPL-PNs fired robustly and consistently to optical activation of Calca^{+} endings in the skin (**Fig. 4D**). The slow latency of these responses was likely not due to slow opsin kinetics, as activation of all endings in the skin, including Aβ-LTMRs, generated faster latency responses (**Extended Data Fig. 9**). Moreover, neurons labeled by *Calca* driver lines did not project to the DCN, as predicted, since direct optical stimulation of the DCN failed to evoke firing in the same VPL-PNs that could be activated by optical stimulation of the skin (**Extended Data Fig. 9**). These optically evoked responses were dependent on the dorsal column, as severing the dorsal column eliminated evoked responses in the DCN (**Extended Data Fig. 9**). Thus, consistent with results of the spinal cord silencing experiments (**Fig. 3K, M**), these findings suggest that high-threshold information is relayed to the DCN by PSDCs that receive

input from HTMRs, either directly or through local interneuron circuits within the spinal cord dorsal horn.

How are receptive fields of DCN projection neurons shaped by the direct and indirect dorsal column pathway inputs? We measured the contributions of the direct and indirect dorsal column pathways to receptive fields of individual VPL-PNs. To do this, we determined Aβ-LTMR input contributions to VPL-PN receptive fields by using vibratory stimuli, as high-frequency vibration is encoded by the direct pathway (**Fig. 4H-I**). In the same experiment, we determined PSDC input contributions to receptive fields of the same VPL-PN neurons using optical activation of Calca$^+$ endings in the skin, because Calca$^+$ neuron inputs to the DCN are conveyed solely by the indirect pathway (**Fig. 4J-K**). Strikingly, the receptive fields of the direct and indirect dorsal column pathway inputs onto VPL-PNs were highly aligned (**Fig. 4L-N**). Responses to gentle vibration were typically restricted to a single digit or 1-2 pads, and optical activation of HTMRs evoked firing only in areas that were sensitive to vibratory stimuli, restricted to the same single digit or 1-2 pads (**Extended Data Fig. 10**). These findings suggest an elaborate somatotopic alignment of the periphery, spinal cord, and DCN: Aβ-LTMRs and HTMRs innervating a small area of skin project into the central nervous system and diverge, with Aβ-LTMRs projecting via the dorsal column directly to the DCN, and both LTMRs and HTMRs activating PSDCs in the spinal cord dorsal horn. Aβ-LTMRs (direct pathway) and PSDCs (indirect pathway) with similar receptive fields then re-converge within the DCN to enable representation of a broad array of tactile features for a single, small area of skin.

DISCUSSION

The dorsal column system enables the perception of a rich array of tactile features[2–4,11]. Models of discriminative touch have focused solely on the roles of LTMR subtypes and their direct dorsal column pathway projections in the creation of these representations[4,9,11]. Here, we demonstrate that PSDCs are an integral, critical component of a brainstem circuit that transforms ascending tactile inputs to produce specialized tactile representations.

Our findings support a new model of the dorsal column discriminative touch pathway **(Extended Data Fig. 11)**. Aβ-LTMRs and the direct dorsal column pathway underlie vibration tuning, whereas PSDC neurons and the indirect dorsal column convey the intensity of sustained stimuli.

Both pathways detect the onset of stimuli and low-threshold responses, together providing exquisite sensitivity. Remarkably, these two components of the dorsal column pathway differentially converge upon distinct DCN-PN subtypes to generate unique combinations of response properties in different sensory streams. Information conveyed to S1 via VPL-PNs emphasize spatial detail, low frequency vibration (<150 Hz), and sustained stimulus intensity. These features are likely generated by prominent input from both Aβ-LTMRs and PSDCs. Tactile signals conveyed to the IC by IC-PNs encode broadband vibratory information (10-500 Hz) rather than spatial detail, and are likely mainly driven by LTMRs, especially Meissner corpuscle/Aβ RA1-LTMRs and Pacinian corpuscle/Aβ RA2-LTMRs. Local interneurons also receive primarily LTMR input to generate surround inhibition in VPL-PNs, and do not fire in response to sustained high-force stimuli, suggesting that they do not receive HTMR input via PSDCs. Similar to the division of LTMRs into subtypes, there may also be physiologically distinct subtypes of PSDCs, given their various contributions to the DCN described here and their heterogeneous response properties in cats[5]. Future work will address potential PSDC subdivisions, as well as how features are represented across a broader range of DCN PN subtypes, such as those that project to the cerebellum and higher-order thalamic nuclei.

We observed striking somatotopic alignment of the direct and indirect dorsal column pathway inputs to the DCN. This alignment enables rich representations in the DCN without compromising spatial detail. The development of this somatotopy likely requires complex coordination between primary sensory neurons, including both LTMRs and HTMRs, spinal cord dorsal horn circuitry, and the DCN. Developmental activity, either spontaneous or mechanically evoked, may play an essential role in organizing this system, as it does in other sensory systems[43,44]. Moreover, adult PSDCs can exhibit robust receptive field plasticity[45,46], raising the possibility that signal propagation via the indirect dorsal column pathway can be modified by sensory experience. Thus, subdivisions of the dorsal column pathway may not only expand the capacity for coding tactile features across DCN output pathways, but may also introduce hard-wired and flexible components to the repertoire of mechanosensory representation in the earliest stages of the sensory hierarchy.

FIGURES

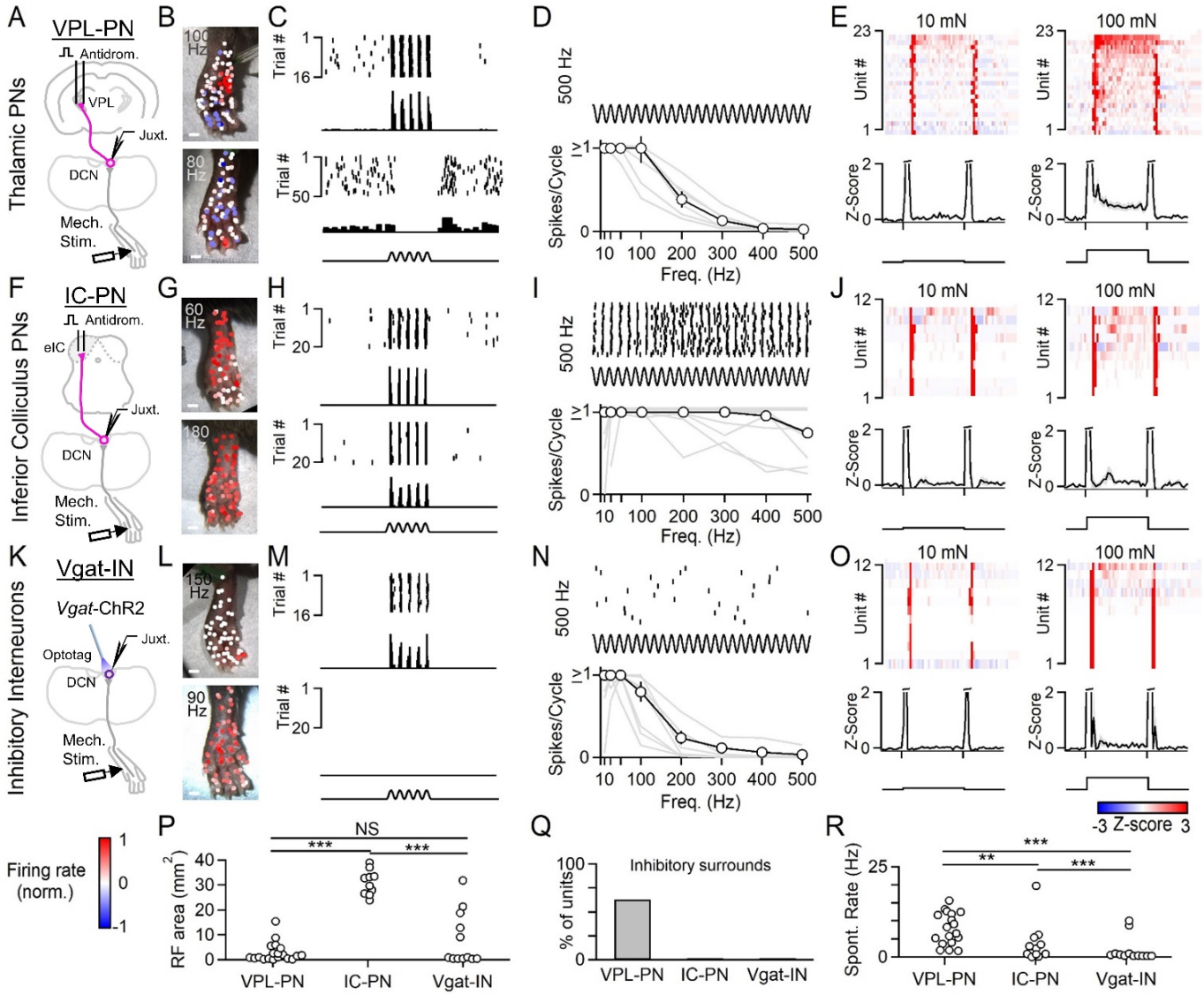

Figure 1: Tactile features are directed to distinct targets in the somatosensory hierarchy

A. Experimental configuration. Juxtacellularly recorded units in the DCN were identified as projecting to the VPL through antidromic activation.

B. Receptive field of VPL-PNs. Each point is a single trial color coded by the unit's firing rate in response to a 100 ms 50 Hz vibration. All scale bars 1 mm. Max firing rate indicated in upper corner.

C. Example trials from B with raster and histogram for two locations of the receptive field for the same unit: an excitatory receptive field (top) and inhibitory surround (bottom). Histograms for excitatory RF are 1 ms bins, inhibitory surrounds 10 ms.

D. Raster of VPL-PN firing in response to a 500 Hz vibration delivered to the excitatory receptive field (top). Vibration tuning of all VPL-PNs with average (black) and individual units (gray).

E. Responses to step indentation to the center of the receptive field for all units (top) and average across units (bottom) for 10 mN (left) and 100 mN (right). Histograms are in 10 ms bins.
F-J. Same as A-E, but for identified IC-PNs. Averages across cells shown with ±SEM.
K-O. Same as A-E, but for optotagged inhibitory interneurons.
P. Excitatory receptive field size for all identified units.
Q. Percent of units with detectable inhibitory surrounds for each cell type.
R: Spontaneous firing rate of all units for each cell type. Number of experiments and statistics in Extended Data Table 1-2.

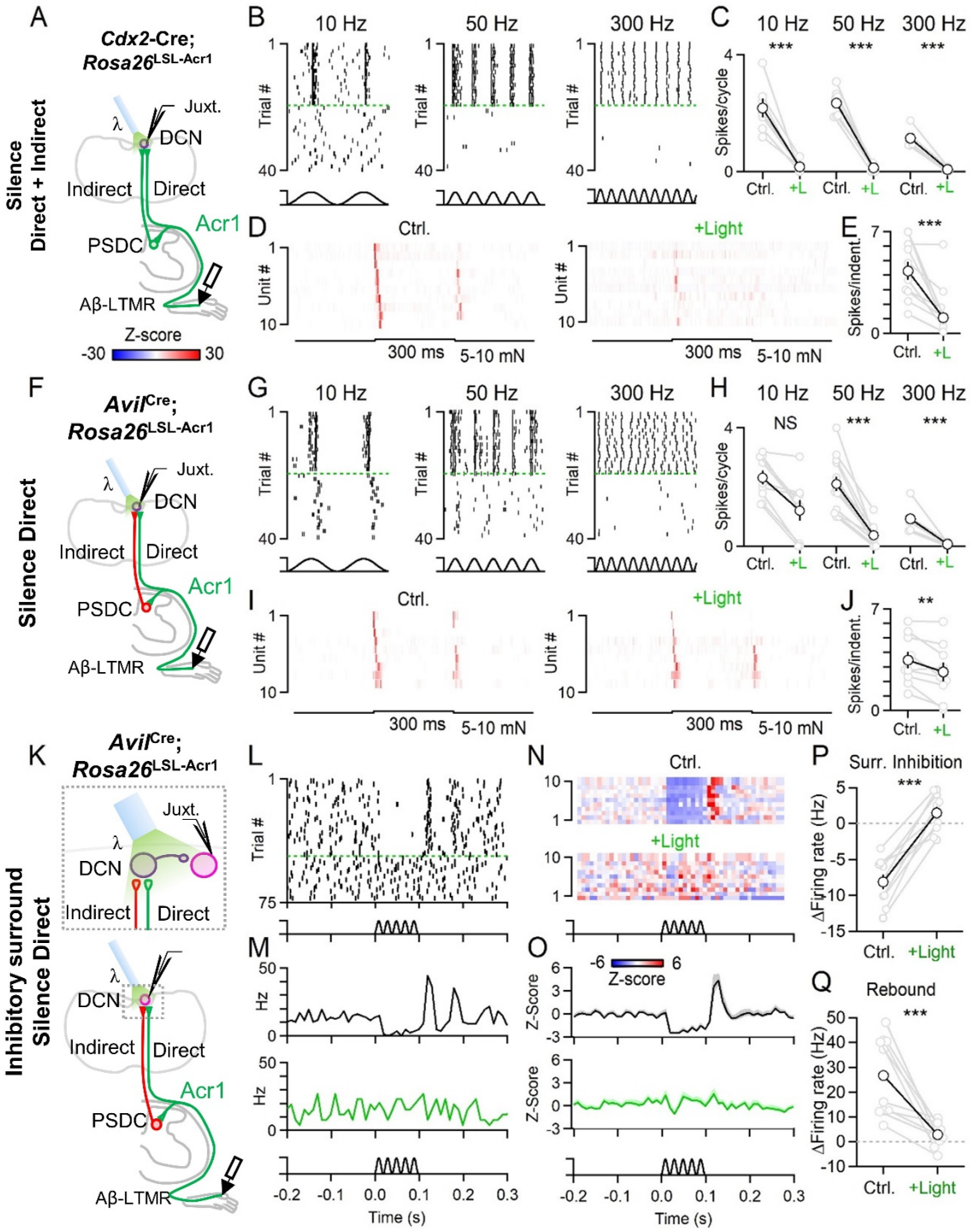

Figure 2: The direct dorsal column pathway conveys high-frequency vibration and fine spatial information to the DCN

A. Acr1 was expressed in both the direct and indirect pathway using *Cdx2-Cre; Rosa26*$^{LSL\text{-}Acr1}$ mice. Light was applied to terminals in the DCN to silence inputs for interleaved trials. 300-400 ms ramps of light preceded 100-200 ms mechanical stimuli. *Cdx2-Cre* drives recombination below C2 (ref.[47]); all spinal cord and DRG neurons below C2 express Acr1.

B. Rasters of DCN neuron responses to 10 (left), 50 (middle) or 300 (right) Hz vibration under normal conditions or when silencing ascending input. Silencing trials sorted and separated by dashed green lines.
C. Average number of spikes per cycle during vibration under normal conditions or during silencing trials for all cells (gray) and average across cells (black).
D. Histograms of responses to indentation under normal conditions (left) and during silencing (right).
E. Average number of spikes triggered by indentation at baseline and when ascending input is silenced.
F. Acr1 expressed in the direct pathway only using *Avil*^{Cre}; *Rosa26*$^{LSL\text{-}Acr1}$ mice; remaining responses in DCN mediated primarily by PSDCs.
G-J. Same as B-E, but when silencing the direct pathway only.
K. Acr1 was expressed in the direct pathway *Avil*^{Cre}; *Rosa26*$^{LSL\text{-}Acr1}$ mice and silenced during stimulation of inhibitory surrounds.
L. Raster of DCN unit during activation of its inhibitory surround with a 50 Hz 100 ms vibration. Silencing trials separated by green dashed line.
M. Histogram of unit in L for control (top) and silencing (bottom) trials. 10 ms bins.
N. Histograms of inhibitory surrounds for all units recorded at baseline (top) and when the direct pathway was silenced (bottom).
O. Average histogram across cells for baseline inhibitory surrounds (top) and when direct pathway was silenced (bottom).
P. Effect of inhibitory surround at baseline or when silencing the direct pathway.
Q. Rebound firing following inhibitory surround at baseline or when silencing the direct pathway.
Summary plots are shown with individual units (gray), and average ± SEM (black).
Number of experiments and statistics in Extended Data Table 1-2.

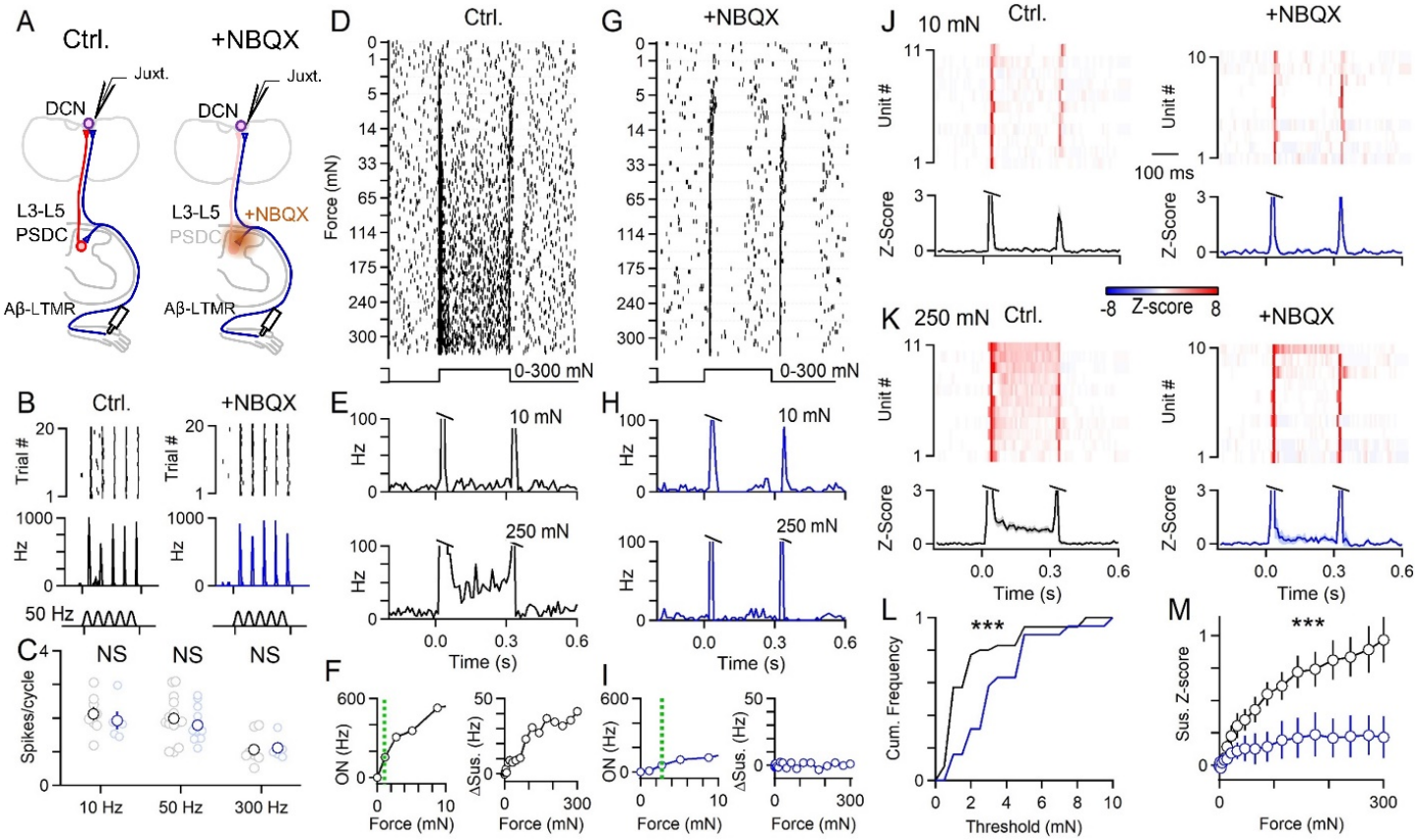

Figure 3: PSDCs and the indirect dorsal column pathway mediate wide dynamic range force intensity tuning in the DCN

A. Experimental configuration. Juxtacellular recordings made from random (for vibration) or putative VPL-PNs (for indentation) in the DCN. A L3-L5 laminectomy was performed to apply MK-801 (10 mM, 10 µL, 5 minutes) followed by NBQX (10 mM, 20 µL, for the recording duration).

B. Example unit response to 50 Hz vibration (10-15 mN) with raster (top) and histogram (bottom) of firing under control conditions (left), and different unit after blockers were applied to the spinal cord (right). 1 ms bins.

C. Summary of vibration responses to units recorded in the presence or absence of blockers.

D. Raster of a single units response to 300 ms step indentation at different forces (0-300 mN or 0-395 kPa) using a blunt probe (1 mm diameter) under control conditions. Trials originally interleaved, but sorted by force for presentation.

E. Histogram of firing for unit in D-F for 10 mN (top) and 250 mN (bottom), 10 ms bins.

F. Right: Max on response (0-20 ms) vs. indentation force. Dashed green line indicates threshold. Right: average sustained firing (100-300 ms) vs. force.

G-I. Same as D-G, but for a different unit and in the presence of blockers.

J. Histograms for all units' responses to 10 mN step indentation (top) and average across units (bottom) under control conditions (left). Responses to different DCN units in the presence of blockers in spinal cord (right). 10 ms bins.

K. Same as J, but for 250 mN step indentation.
L. Cumulative histogram of on response threshold for all units in control conditions (black) and for units in the presence of blockers (blue).
M. Average sustained firing rate for units under control conditions (black) and for units in the presence of blockers (blue).
Summary plots are shown with individual units (light), and average ± SEM (dark).
Number of experiments and statistics in Extended Data Table 1-2.

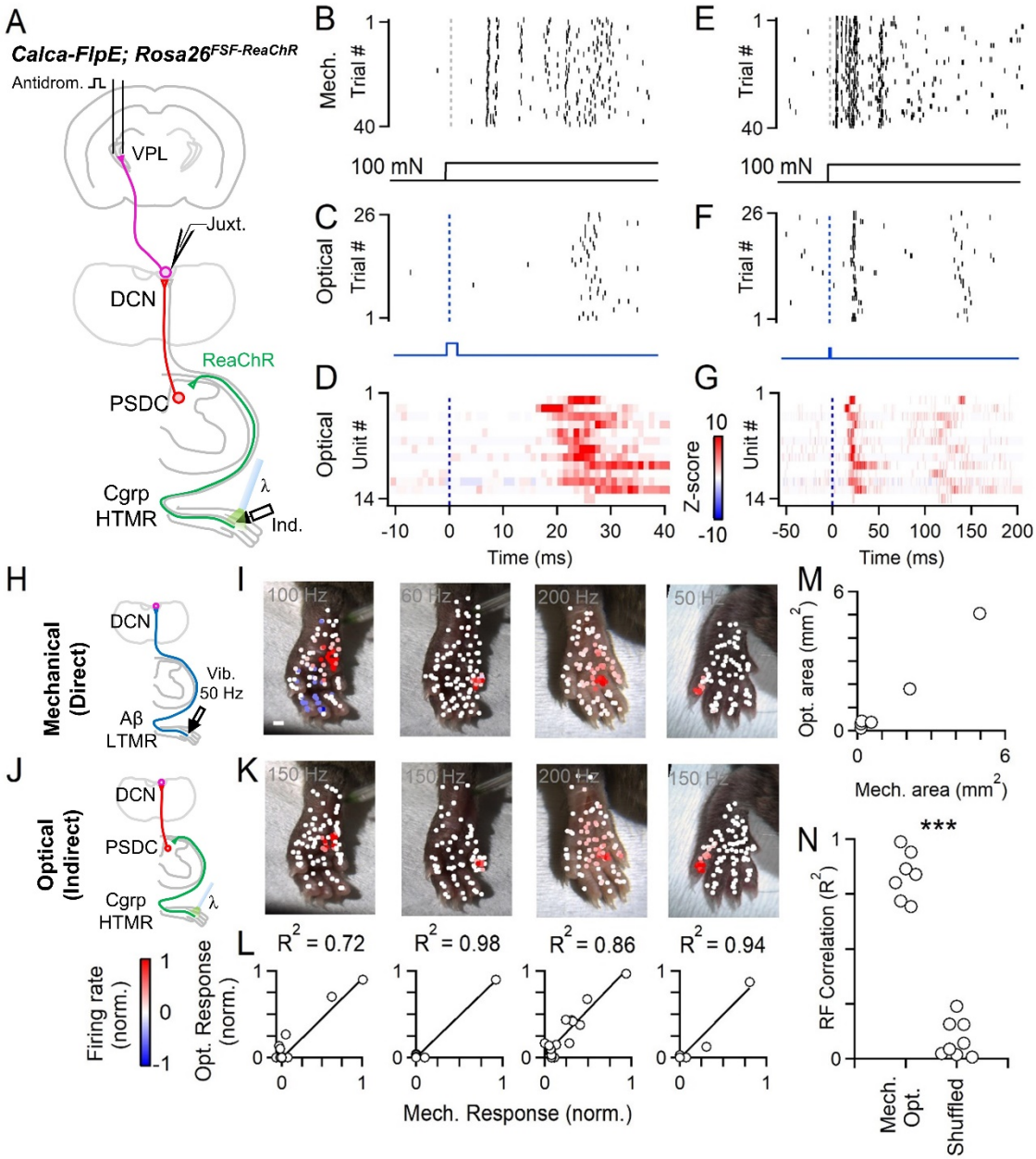

Figure 4: Somatotopic convergence of the direct and indirect dorsal column pathways onto individual VPL-PNs

A. Experimental configuration. VPL-PNs were identified with antidromic activation in *Calca-FlpE*; *Rosa26*$^{FSF\text{-}ReaChR}$ animals. A fiber optic activated ReaChR in *Calca* HTMRs in the hindlimb.

B. Raster of a VPL-PN response to intense indentation.

C. VPL-PN from B in response to optical activation (2 ms, 60 mW/mm2) of HTMRs in the skin.

D. Histogram for all VPL-PNs and their response to optical activation of HTMRs in the skin. 1 ms bins.

E-G. Same as B-D, but expanded timescale.

H. A 50 Hz 100 ms vibration was applied to different points on the skin for putative VPL-PNs in *Calca-FlpE*; *Rosa26*$^{FSF\text{-}ReaChR}$ animals.

I. Vibration receptive field maps for four putative VPL-PNs. Each point is a single trial color coded by its normalized mechanically evoked firing rate.
J. For same units in H-I, light pulses (5 pulses at 0.5 Hz, 2 ms, 60 mW/mm^2) were applied to different points on the skin.
K. Optical receptive field for same units in I. Each point is a single trial color coded by its normalized optically evoked firing rate.
L. Correlation of optical and mechanical responses. Each point is the average mechanically and optically evoked responses for a single region of skin.
M. Area of optically evoked receptive field vs. area of mechanically evoked receptive field for single units. Each point is one DCN unit.
N. Correlation coefficients (R^2) of optically- and mechanically evoked receptive fields within individual units, or R^2 of receptive fields shuffled between units.
Number of experiments and statistics in Extended Data Table 1-2.

EXTENDED DATA FIGURES

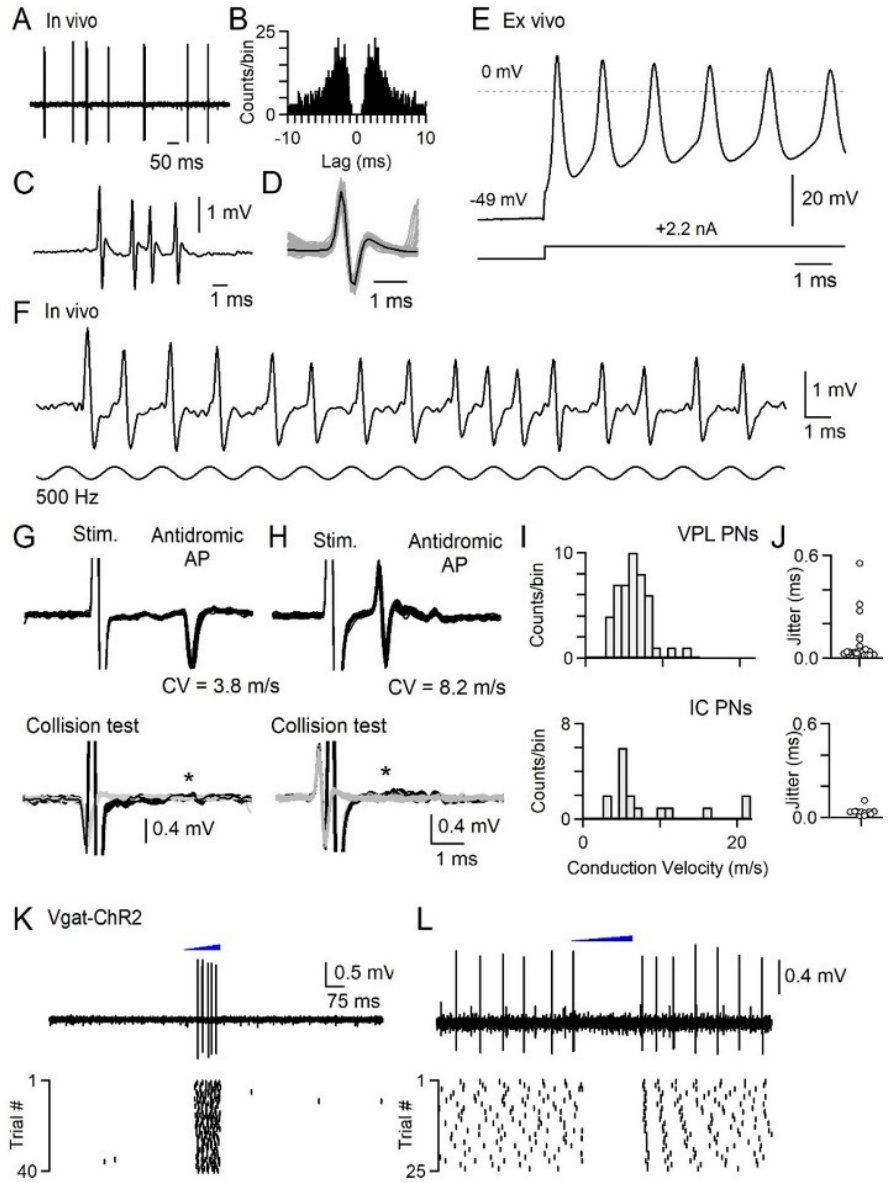

Extended Data Fig. 1: Juxtacellular recording in the DCN, antidromic activation, and optotagging

Juxtacellular recordings were made from units in the gracile nucleus of the DCN to obtain high signal-to-noise recordings of putative single units. Units in the DCN can fire at very high rates up to 1 kHz and can undergo use-dependent changes in action potential waveforms during bursts[48]. Response properties in the DCN have been shown to be relatively insensitive to anesthetics, and the distribution of response properties are similar between anesthetized and non-anesthetized preparations[17,49,50].

A. Example of spontaneous firing recorded juxtacellularly in the DCN in vivo.

B. Autocorrelogram for unit in A-D.

C. Example high frequency burst.
D. Overlaid spikes with single events (gray) and average waveform (black).
E. Ex vivo intracellular recording of a DCN neuron from an intact brainstem of an adult mouse. Recording was performed in near-physiological conditions (35°C). A current injection was supplied to trigger a brief burst of very high frequency firing. Cells could fire up to 1 kHz bursts with use-dependent changes in action potential waveform as observed in vivo.
F. Juxtacellular recording of a single DCN unit in vivo showing response to high frequency (500 Hz) vibration of the hindlimb. The unit could entrain to single cycles of the vibration and underwent use-dependent changes in waveform. Vibration begins 6 ms prior to displayed time window.
G. Top: A unit in the DCN antidromically activated from the VPL. Overlay of 20 trials shows consistent waveform of the stimulus artifact (stim.) and antidromic action potential (Antidromic AP). The conduction velocity was calculated from the latency to spike following the stimulus artifact with an estimated distance of 9.8 mm. Bottom: during a collision test, the stimulus was triggered from the spontaneous firing of the unit. Overlay of 20 trials when electrical stimuli were triggered from spontaneous firing (black). In these trials, stimulation failed to evoke an antidromic spike that would be expected at the latency indicated by the asterisk. Waveform of spontaneous firing in which stimuli were not triggered are overlaid in gray.
H. Same as in G, but for a different example unit with faster conduction velocity.
I. Histogram of calculated conduction velocities for units antidromically activated from the VPL (top) and external cortex of the inferior colliculus (IC, bottom). Distance from the DCN to VPL was estimated to be 9.8 mm. Distance from the DCN to IC was estimated to be 9.4 mm. IC units are type 1 only (see Extended Data Figure 2).
J. Jitter (standard deviation) of latency from units antidromically activated from the VPL (top) or IC (bottom).
K. Optotagging of inhibitory interneurons in the DCN in a Vgat-ChR2 mouse. A fiber optic was positioned above the DCN (400 µm diameter, 1 mm away). Light from a fiber coupled LED was ramped for 200-300 ms (470 nm, 1-2 mW/mm^2). Optotagged units fired during the ramp. A single trial (top) and raster of all trials (bottom) for an optotagged unit are shown.
L. Units that were not optotagged were suppressed by light ramps, or fired rebounds after termination of the ramp.

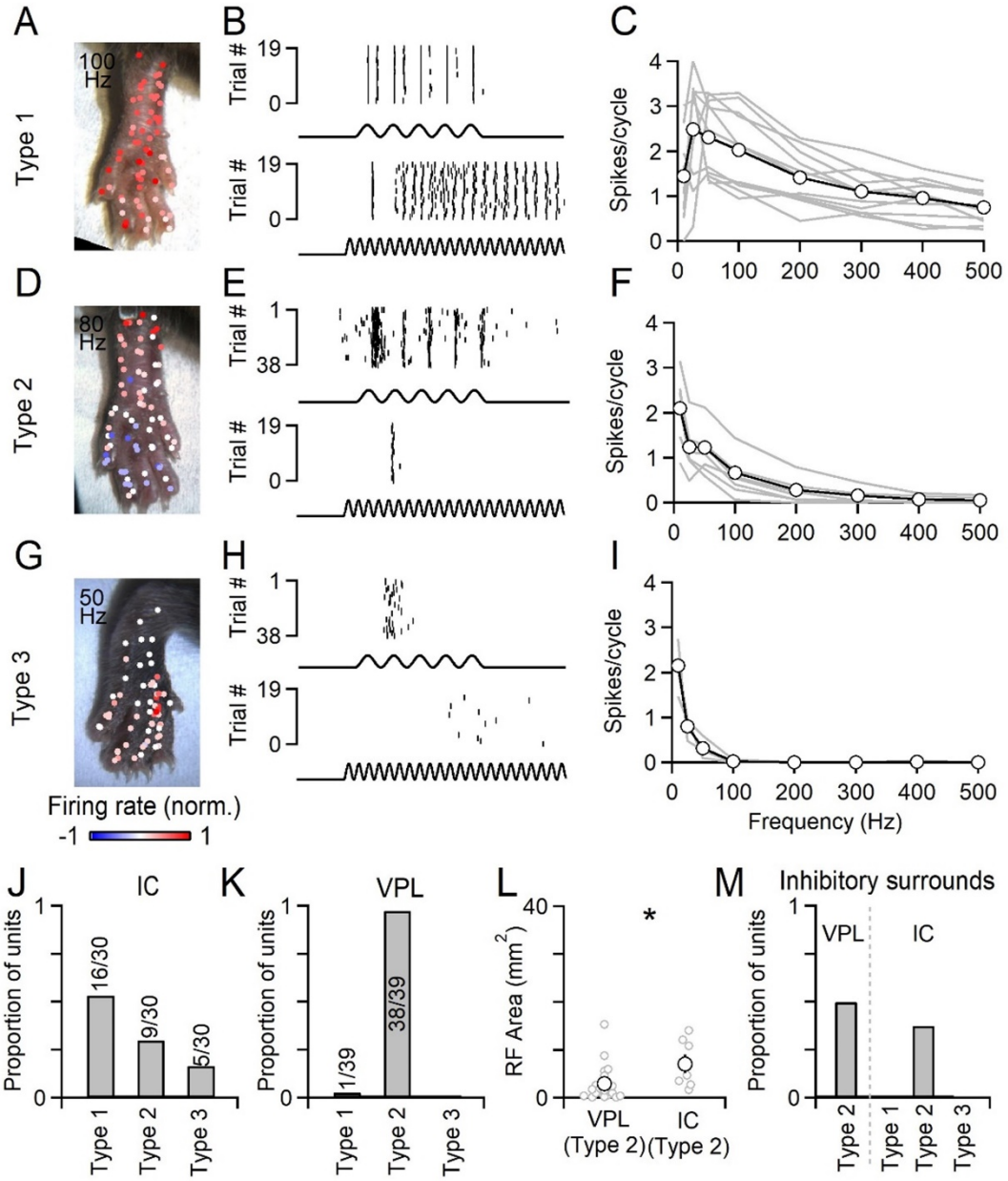

Extended Data Fig. 2: IC projection neuron subtypes

The DCN is composed of several types of projection neurons and local interneurons. VPL-PNs are the most abundant, with an estimated proportion of VPL-PN:IC-PN:Vgat+ neuron of 2:1:1 based on retrograde tracing and genetic labeling in mice[13], and larger proportions of VPL-PNs reported in another study[12]. Units that could be antidromically activated from the IC or VPL fell into three functional types with distinct properties. Type 1 units have very large receptive fields that include almost the entire hindlimb, they can entrain their firing to very high frequencies (>300 Hz and often up to 500 Hz), and do not have inhibitory surrounds. The broad receptive field and entrainment to high frequencies suggest that they receive strong input from Pacinian corpuscles. These units typically projected to the IC. Type 2 units had small receptive fields,

typically consisting of 1-2 digits or pads, or a small portion of the heel. They often had inhibitory surrounds, and could entrain their firing to modest vibration frequencies (up to 100-200 Hz). These units could not entrain their firing to vibration frequencies >300 Hz even at high forces. Almost all VPL-PN units were classified as type 2. Units projecting to the IC that were classified as type 2 had larger receptive fields compared to type 2 units projecting to the VPL, and were a smaller proportion of IC projecting units. Type 3 units had receptive field sizes similar to type 2 units, but were poorly activated by vibration. They were very sensitive and exclusively responsive to the initial contact of a stimulus. A small proportion of units activated from the IC were classified as type 3.

A. Example receptive field of a type 1 ICPN.

B. Example rasters of type 1 IC unit in response to 50 (top) or 500 Hz (bottom) vibration.

C. Responsiveness of type 1 IC units to different vibration frequencies. Data is shown for individual units (gray) and average across units (black).

D-F. Same as A-C, but for type 2 units.

G-I. Same as A-C, but for type 3 units.

J. Distribution of functional types for units antidromically activated from the IC.

K. Distribution of functional types for units antidromically activated from the VPL.

L. Receptive field area for type 2 units antidromically activated from the IC or VPL. Distributions are significantly different ($p < 0.001$, Kolmogorov-Smirnov test). Individual units (gray) and average ± SEM (black).

M. Proportion of units with inhibitory surrounds for each functional type.

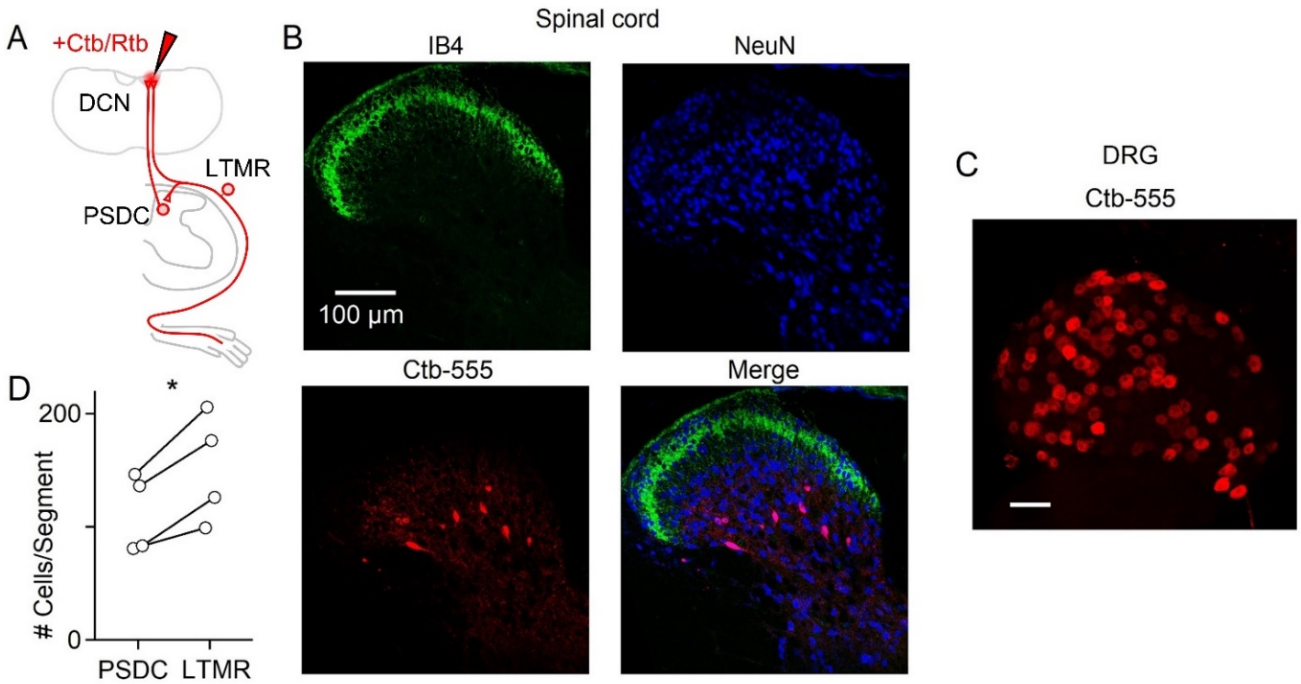

Extended Data Fig. 3: Prevalence and anatomical location of PSDCs.
Choleratoxin-B (Ctb) or Retrobeads (Rtb) were injected into the DCN or C1 DC to label PSDCs and Aβ-LTMRs that project to the DCN. The number of LTMRs and PSDCs per thoracic spinal segment within the same animal were compared. PSDCs were found in lamina III-IV as described by others[33,34,51].
A. Schematic showing injection of retrograde tracer into the brainstem and uptake by either PSDCs in the dorsal horn of the spinal cord or Aβ-LTMRs in the DRG.
B. 10 µm Z-projection of a transverse thoracic spinal cord section (60 µm thick) with immunofluorescence of IB4 (top left, green), NeuN (top right, blue), Ctb-555 (bottom left), and merged images (bottom right).
C. Single plane image of a whole-mount thoracic DRG containing sensory neurons labeled with Ctb-555 from the same animal shown in B.
D. Comparison of number of Ctb or Rtb labeled cells in the thoracic spinal cord. Each marker pair is the average from one animal, showing the average number of cells labeled in 1-2 DRGs, and the number of PSDCs estimated to exist in one spinal segment (1000 µm length of spinal cord) based on the average number of PSDCs labeled in 10-20 spinal sections (60 µm thickness).

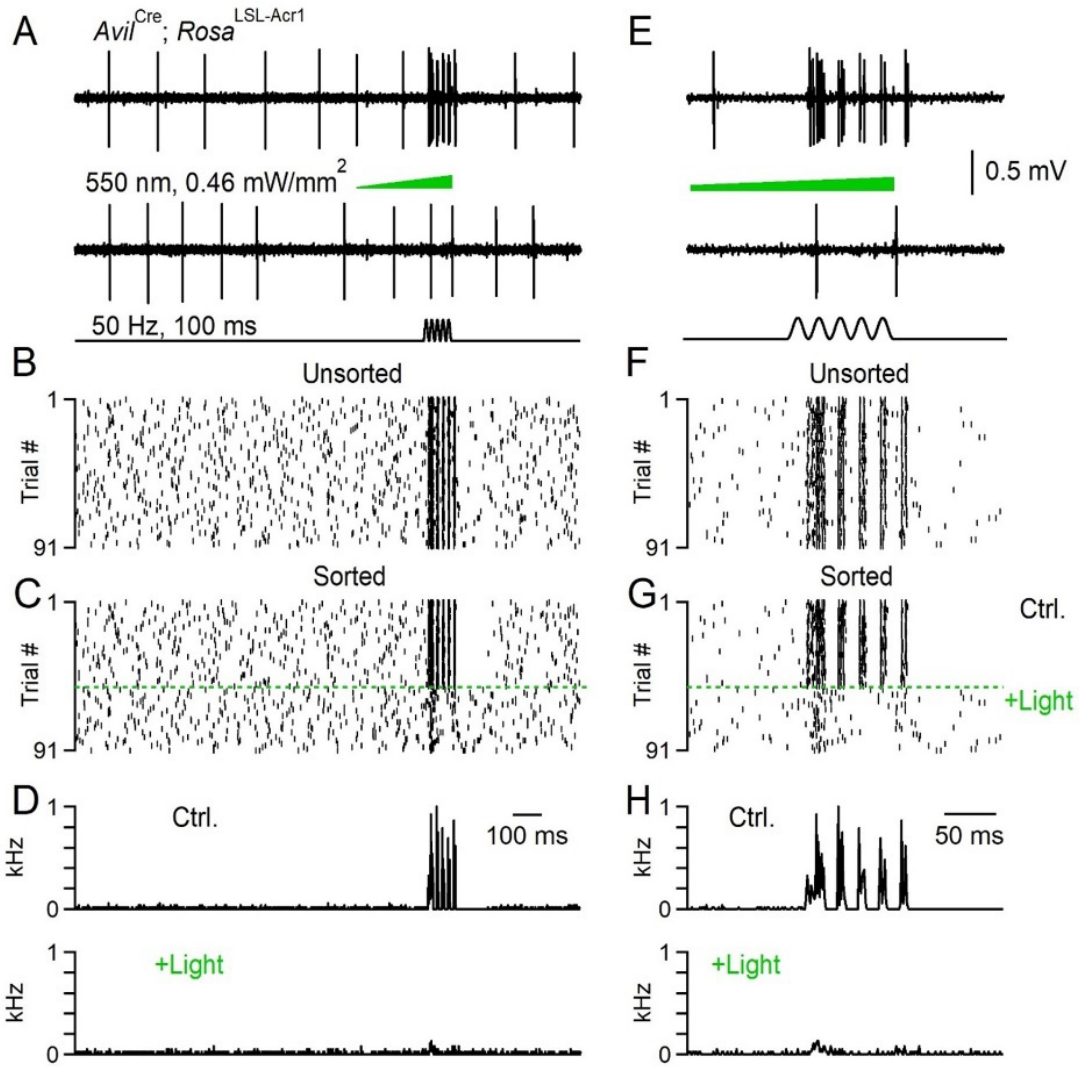

Extended Data Fig. 4: Silencing sensory neuron terminals using Acr1.

A. Example juxtacellular recording from a DCN unit in an *Avil*^{Cre}*; Rosa26*$^{LSL\text{-}Acr1}$ animal. A 50 Hz, 100 ms 10-15 mN vibration was applied to the center of the receptive field of the DCN unit (top). On some trials, light (550 nm, 0.46 mW/mm2) was applied to the surface of the brainstem by a fiber optic (400 µm diameter, 1 mm away). The light was ramped over the course of 350 ms.

B. Raster of all trials for unit shown in A. Control and light ramp trials were interleaved.

C. Raster for unit shown in A and B, but trials are sorted for whether light was on (Control, Ctrl.) or off (+Light). Separation of Ctrl. and +Light trials indicated by green dashed line.

D. Histogram of firing for unit shown in A-C for control trials (Ctrl, top) and when light was applied (+Light, bottom). Bin size is 1 ms.

E-H. Same unit as A-D, but with expanded time window around the time of mechanical stimulation.

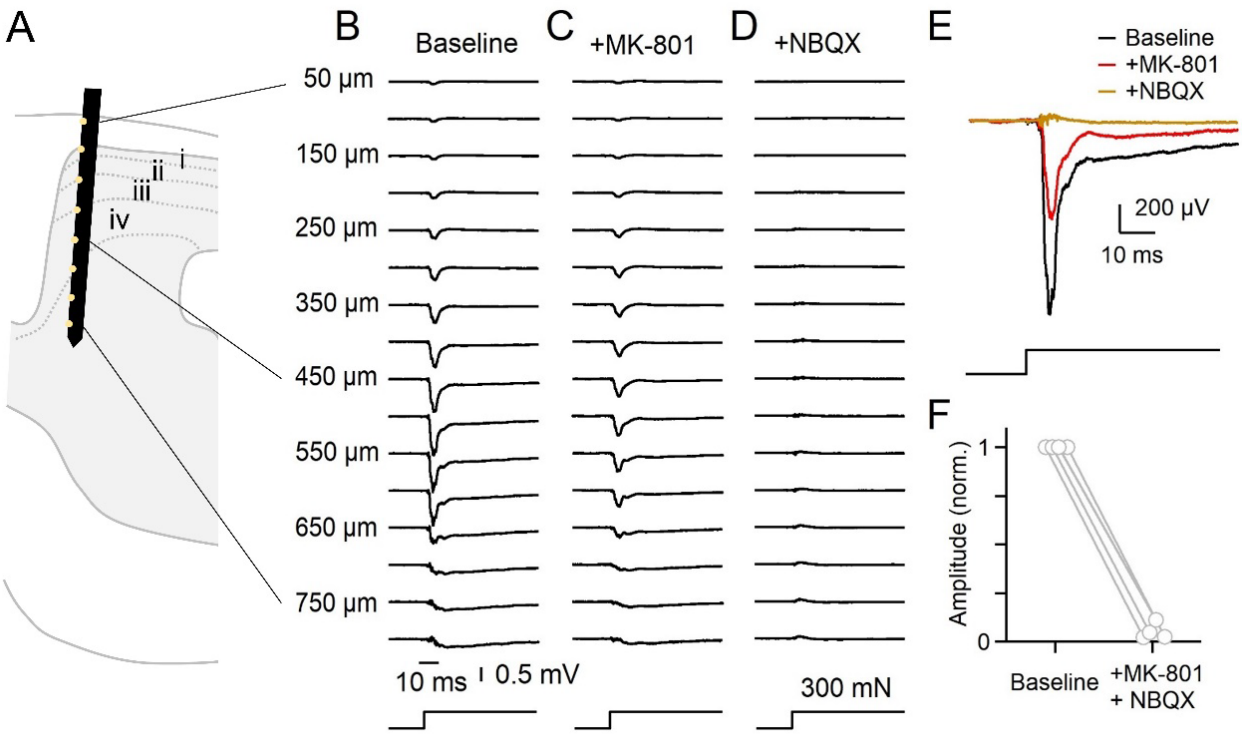

Extended Data Fig. 5: Blockade of glutamatergic transmission suppresses hindlimb responses in the spinal cord

An MEA was inserted into L4 spinal dorsal horn, with recording sites facing medially. Field potentials were recorded in response to a 300 mN step applied to the center of the receptive field on the hindlimb. Following baseline trials, MK-801 (10 mM, 10 µL) was applied to the surface of the spinal cord for 3-5 minutes to block NMDA receptors. The surface was then irrigated with saline and NBQX (10 mM, 20 µL) was applied to block AMPA receptors.

A. Schematic of approximate recording location. MEA has 16x2 recording sites spaced 50 µm apart. Only a subset of sites are schematized.

B. Field potentials generated at various depths of the spinal cord in response to a 300 mN step indentation under baseline conditions.

C. Same recording as in B-E, but after application of MK-801 to the surface of the spinal cord.

D. Same recording as in B-E, but after application of NBQX to the surface of the cord.

E. Overlaid field potentials from 450 µm depth recording site in response to 300 mN indentation from recording in B-D. Responses following NBQX remained suppressed for the remainder of the recording (30 minutes after NBQX application).

F. Summary of change in evoked amplitude. Each marker pair is one animal.

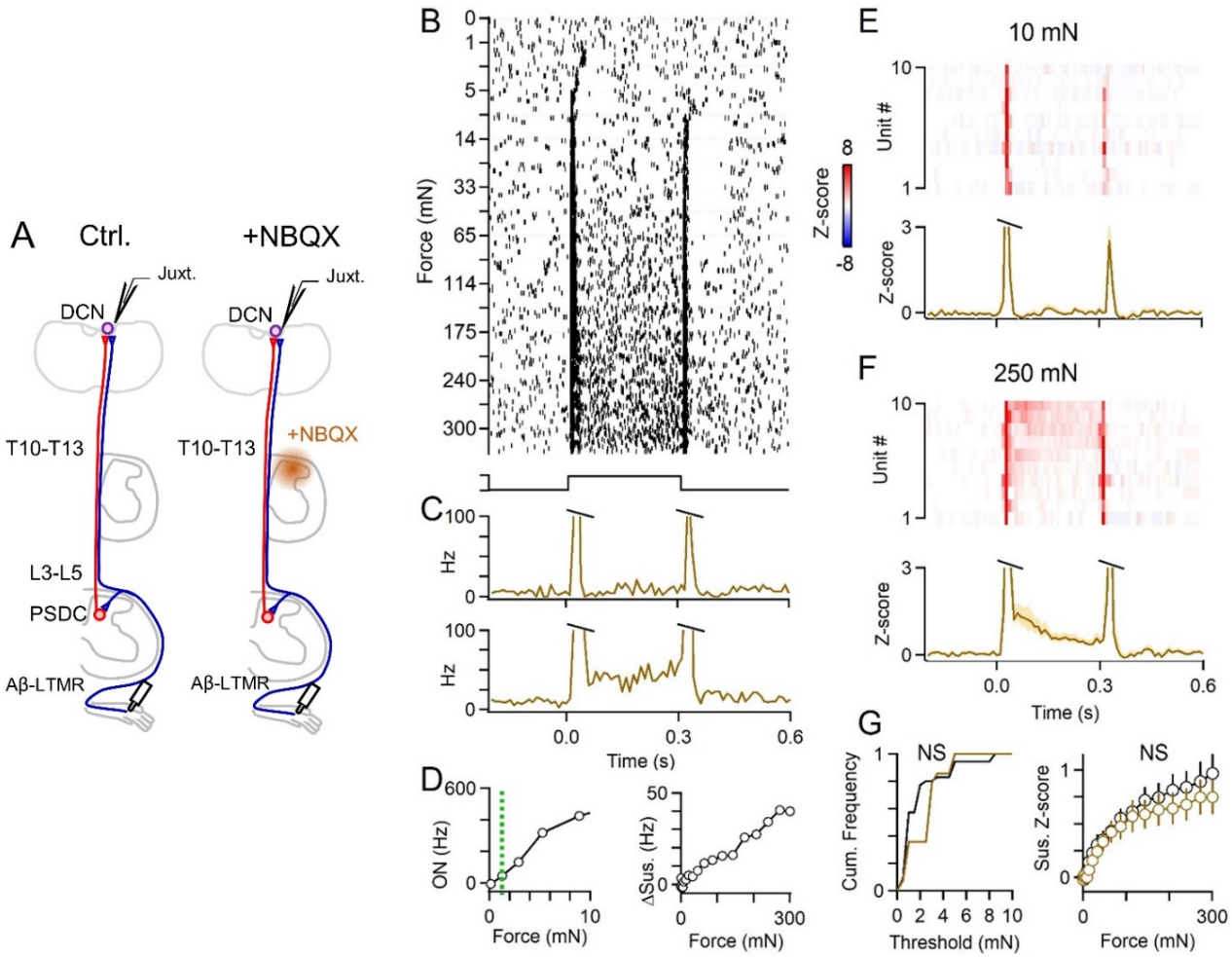

Extended Data Fig. 6: Pharmacological blockade of thoracic spinal cord does not alter hindpaw responses in the DCN.

Pharmacological manipulations can have non-specific effects, as drugs may spread from the site of application or enter the body systemically. We assessed these possibilities by applying glutamatergic antagonists to the thoracic and upper lumbar cord (T10-T13) to determine whether hindlimb responses in the DCN may be altered through diffusion of the drug to the DCN or non-targeted regions of the spinal cord. A laminectomy was performed over the T10-T13 spinal segments, and the dura was removed. MK-801 (10 mM; 10 µL) was first applied to the surface of the spinal cord for 5 minutes. The cord was then abundantly irrigated with saline. NBQX (10 mM; 20 µL) was then applied to the surface and gelfoam was placed on top and kept moist with saline.

A. Schematic of experimental setup.

B. Raster of example putative VPL-PN unit in response to step indentations of various forces (0-300 mN) in the presence of NBQX over T10-T13 spinal segments.

C. Histogram of average responses to 10 mN (top) and 250 mN (bottom) for unit shown in B-D.

D. Left: Max on response (0-20 ms) vs. indentation force. Dashed green line indicates threshold. Right: average sustained firing (50-250 ms) vs. force.

E. Top: Response of DCN units to 10 mN step indentation in the presence of NBQX. Bottom: Average across DCN units to 10 mN indentation in the presence of NBQX.
F. Same as E, but for 250 mN step indentation.
G. Left: Mechanical threshold of on-response for units in the presence (brown) or absence (black) of NBQX over T10-T13 spinal segments. Distributions are not significantly different (Kolmogorov-Smirnov test, $p = 0.25$). Right: Average ± SEM of sustained firing rate as a function of indentation force across cells in the presence (brown) or absence (black) of NBQX over the T10-T13 spinal segments.

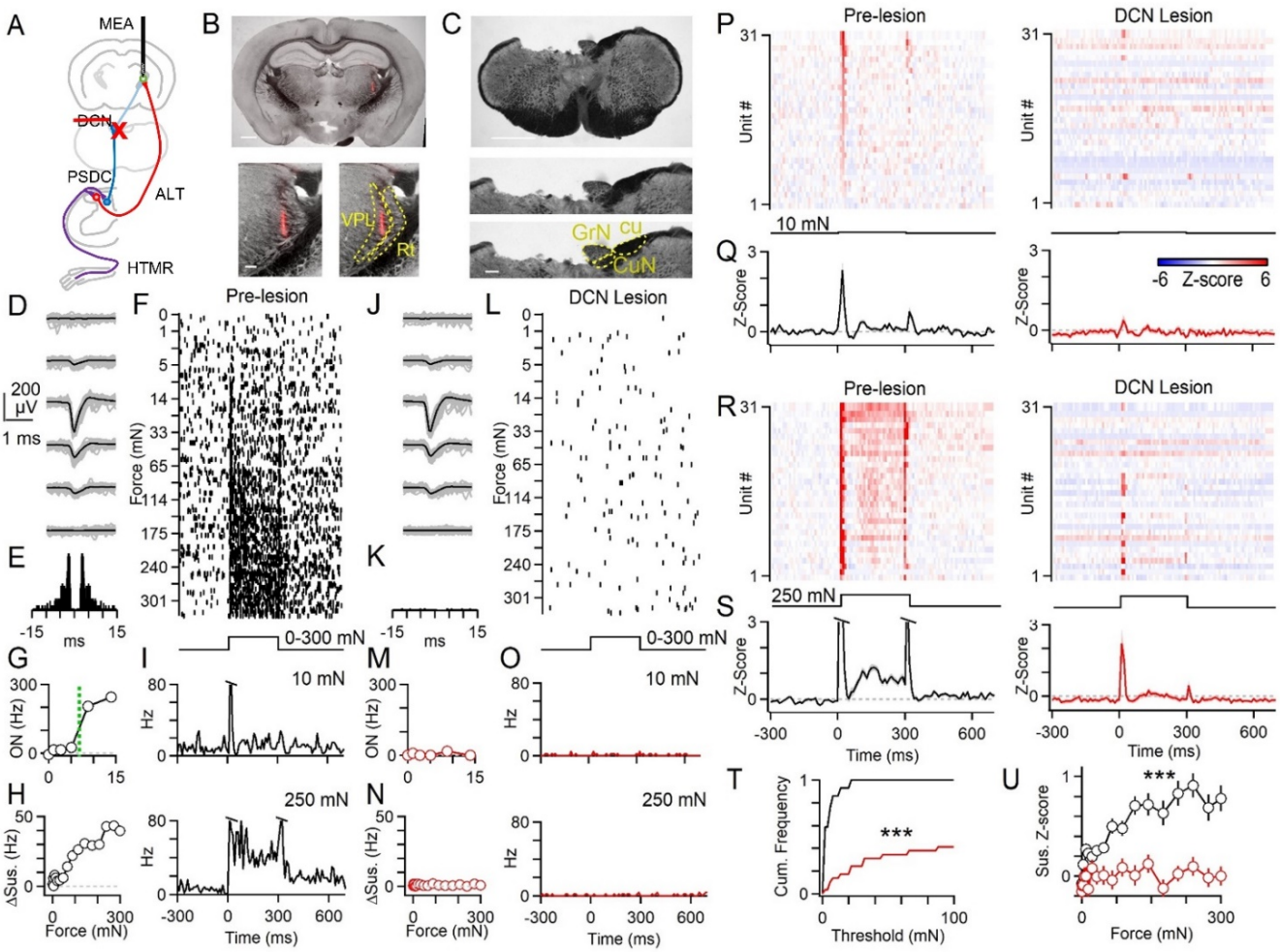

Extended Data Fig. 7: The DCN supplies high force information to the middle VPL (mVPL).

The primary somatosensory thalamus can be subdivided in to rostral, middle and caudal regions [52]. Rostral regions may receive more proprioceptive input and has large receptive fields, the middle region has cutaneous responses with detailed spatial receptive fields, and the caudal region has diffuse receptive fields and may be more responsive to intense or nociceptive stimuli. We asked whether the mVPL can the intensity of sustained stimuli, and whether such coding arises from the anterolateral tract (ALT) or the dorsal column system. The dorsal column system crosses just rostral to the DCN, whereas the ALT crosses within the spinal cord and runs laterally. Other spinothalamic and ascending neurons also cross within the spinal cord and run along the ventral aspect of the brainstem, and should be spared.

A. Schematized experimental configuration. A 32-channel multi-electrode array (MEA) was inserted into the middle VPL of the right thalamus. Mechanical indentation of the contralateral (left) hindpaw was performed before and after lesion of the left DCN by aspiration. The lesion should disrupt DCN input from reaching the VPL, but spare input from ALT neurons.

B. Coronal section of the brain (50 µm) following recording with DiI labeling from the MEA in the right VPL (top). Inset shows magnified view of the thalamus (bottom left) and inferred location of VPL and thalamic reticular nucleus (Rt, bottom right).
C. Coronal section of the brainstem showing the location of the lesion. The dorsal brainstem was aspirated at the level of the caudal DCN on the left side (top). Inset shows magnified view of the lesion site, and location of the gracile nucleus (GrN) that relays information from the hindpaw, and also the cuneate tract (cu) and some of the cuneate nucleus (CuN).
D. Waveform for a unit recorded across four channels of the MEA prior to the DCN lesion with a subset of single events (gray) and overlaid average (black).
E. Autocorrelogram for unit shown in D-O prior to the lesion.
F. Raster of firing for unit shown in D-O in response to a 300 ms step indentation of varying force. Trials were interleaved, but are shown sorted for presentation.
G. Maximum firing rate for the onset of step indentation (0-50 ms) as a function of indentation force for unit shown in D-O prior to lesion. Dashed green line indicates the measured threshold.
H. Average firing rate during the sustained component of the step indentation (150-300 ms) for unit shown in D-O prior to lesion.
I. Time course of firing rate for unit shown in D-O in response to indentation for 10 mN (top) and 250 mN (bottom) prior to lesion.
J-O. Same as D-I, but for the same unit after DCN lesion.
P. Average histograms for all mVPL units in response to 10 mN 300 ms indentation prior to lesion (left) and for the same units after DCN lesion (right). Units are sorted by strength of on-response to 10 mN indentation.
Q. Average histogram of all mVPL units in response to 10 mN indentation before (left) and after (right) lesion of the DCN.
R. Average histograms for all mVPL units in response to 250 mN 300 ms indentation prior to lesion (left) and for the same units after DCN lesion (right). Units are same as shown in P, but sorted by strength of sustained response at 250 mN.
S. Average histogram of all mVPL units in response to 250 mN indentation before (left) and after (right) lesion of the DCN.
T. Cumulative histogram of on-response threshold for the same units before (black) and after (red) lesion of the DCN. About 60% of units could no longer be activated by indentations up to 300 mN following DCN lesion.
U. Average ± SEM of sustained response of all units as a function of indentation force before (black) and after (red) lesion of the DCN.

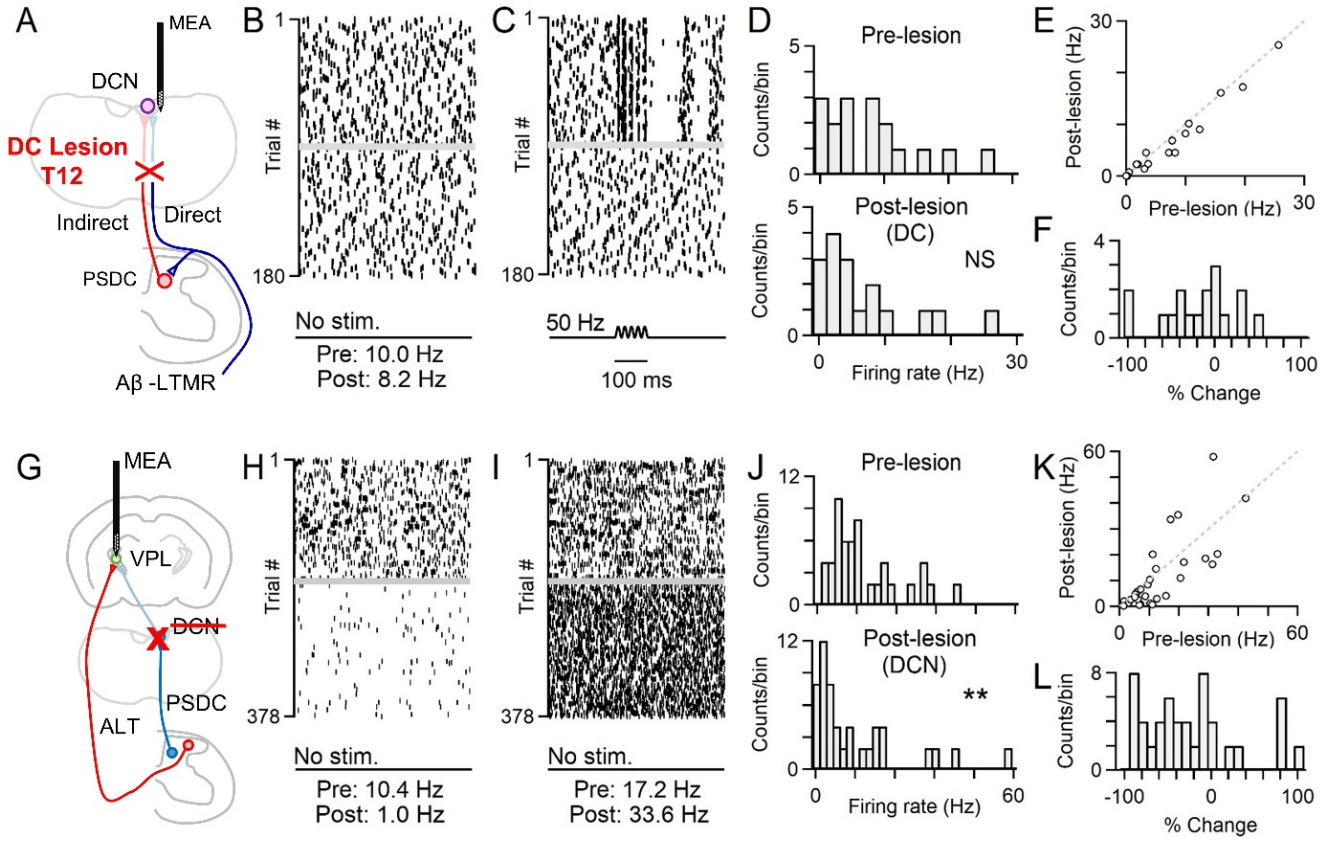

Extended Data Fig. 8: PSDCs do not drive spontaneous firing in the DCN; DCN drives spontaneous firing in some middle VPL neurons

Most VPL-PNs in the DCN are spontaneously active, and it is unclear whether this spontaneous activity is intrinsic to the DCN or is generated by input from the spinal cord. Lesioning the DC had no statistically significant effect on spontaneous firing for randomly recorded neurons in the gracile. Upstream, neurons in the VPL are also spontaneously active, and it is unclear whether spontaneous firing the mVPL is driven by spontaneous firing in the DCN. We found that lesioning the DCN had complicated effects on the VPL. Although there was no net effect on spontaneous activity, most units underwent changes in spontaneous firing rate following lesion of the DCN, and the distribution of spontaneous firing rates in the mVPL was significantly different following DCN lesion. These experiments may be complicated by the fact that lesioning the DCN also likely destroys descending corticospinal input to the spinal cord.

A. Experimental configuration. A high-density 32-channel MEA was inserted into the hindpaw region of the gracile nucleus. A laminectomy was performed at T12. After 10 minutes of baseline recording, a needle was used to sever the dorsal column.
B. Spontaneous firing of a DCN unit. Gray line indicates time of the lesion.
C. Evoked firing of unit shown in B in response to 50 Hz 100 ms vibration applied to the excitatory receptive field in the hindpaw. Full lesioning of the dorsal column was confirmed by elimination of touch-evoked responses.

D. Distribution of spontaneous firing rates for DCN units prior to lesion (top) and for the same units after lesioning the dorsal column (bottom). The distributions are not significantly different (Kolmogorov-Smirnov test, $p = 0.93$).

E. Post-lesion firing rate as a function of pre-lesion firing rate for all units. Each point is one unit.

F. Percent change of firing rate for DCN units after lesion of the DC.

G. A 32-channel MEA was inserted into the middle VPL. The DCN was exposed. After baseline recording and step indentation, the DCN contralateral to the recording was either aspirated or a single cut across the gracile was made with a needle.

H. Raster for a single unit with spontaneous firing before and after lesion of the DCN. Gray line indicates time of the lesion.

I. Same as H, but for a different unit in the same recording.

J. Distribution of spontaneous firing rates for mVPL units prior to lesion (top) and for the same units after lesioning the DCN (bottom). Distributions are significantly different (Kolmogorov-Smirnov test, $p = 0.0014$).

K. Post-lesion firing rate as a function of pre-lesion firing rate for all units. Each point is one unit.

L. Percent change of firing rate for mVPL units after lesion of the DCN.

Extended Data Fig. 9: Calca$^+$ HTMRs do not project directly to the DCN but they do drive long latency responses

Calca is expressed in a broad set of sensory neurons. These include mechanically sensitive and polymodal receptors that have A or C-fiber conduction velocity, and have higher mechanical thresholds than Aβ-LTMRs[39–42]. Calca$^+$ DRG neurons do not project to the DCN[36].

A. Left: Random DCN neurons were juxtacellularly recorded in the DCN in a *Calca*^{CreER}; *Avil-FlpO*; *Rosa26*$^{LSL\text{-}FSF\text{-}ReaChR}$ animal. Light was restricted to a small area of skin on the hindpaw. Right: Histogram of evoked firing for units in the DCN following optical stimulation of the skin.

B. Left: The same DCN neurons were recorded with light now applied to the DCN. If sensory neurons labeled by *Calca*^{CreER} project to the brainstem, their terminals should be optically excitable in the DCN. Right: Histogram of evoked firing for same units shown in A following optical stimulation of the DCN. Same units as shown in A.

C. Histogram of DCN units in response to strong mechanical indentation beginning at time 0, in a wildtype animal.

D. Response of DCN neurons to optical activation of the skin in animal expressing ReaChR in all sensory neurons. Pulse (2-5 ms) starts at time 0.

E. Response of DCN neurons to optical activation of the skin in animal expressing ReaChR in Calca$^+$ neurons.

F. Response of DCN neurons to optical activation of the skin in animal expressing ReaChR in Calca$^+$ neurons after lesioning the DC. Units are different from those in E.

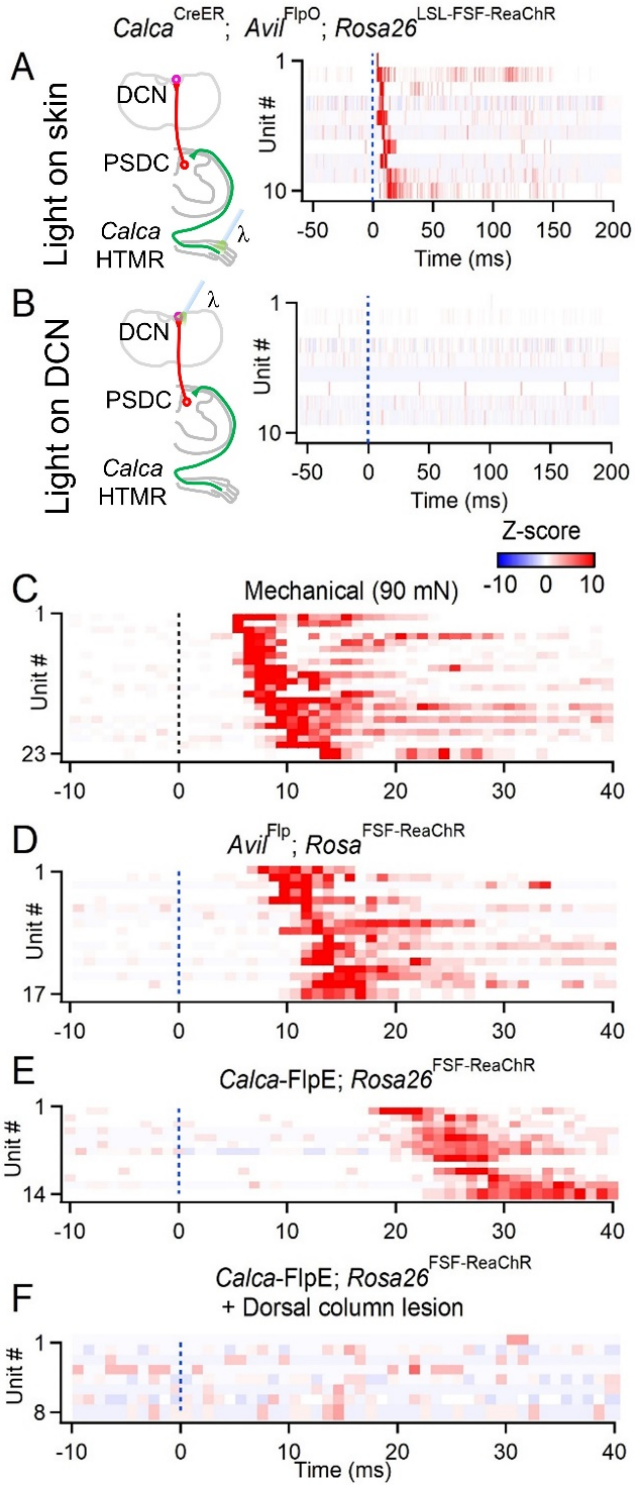

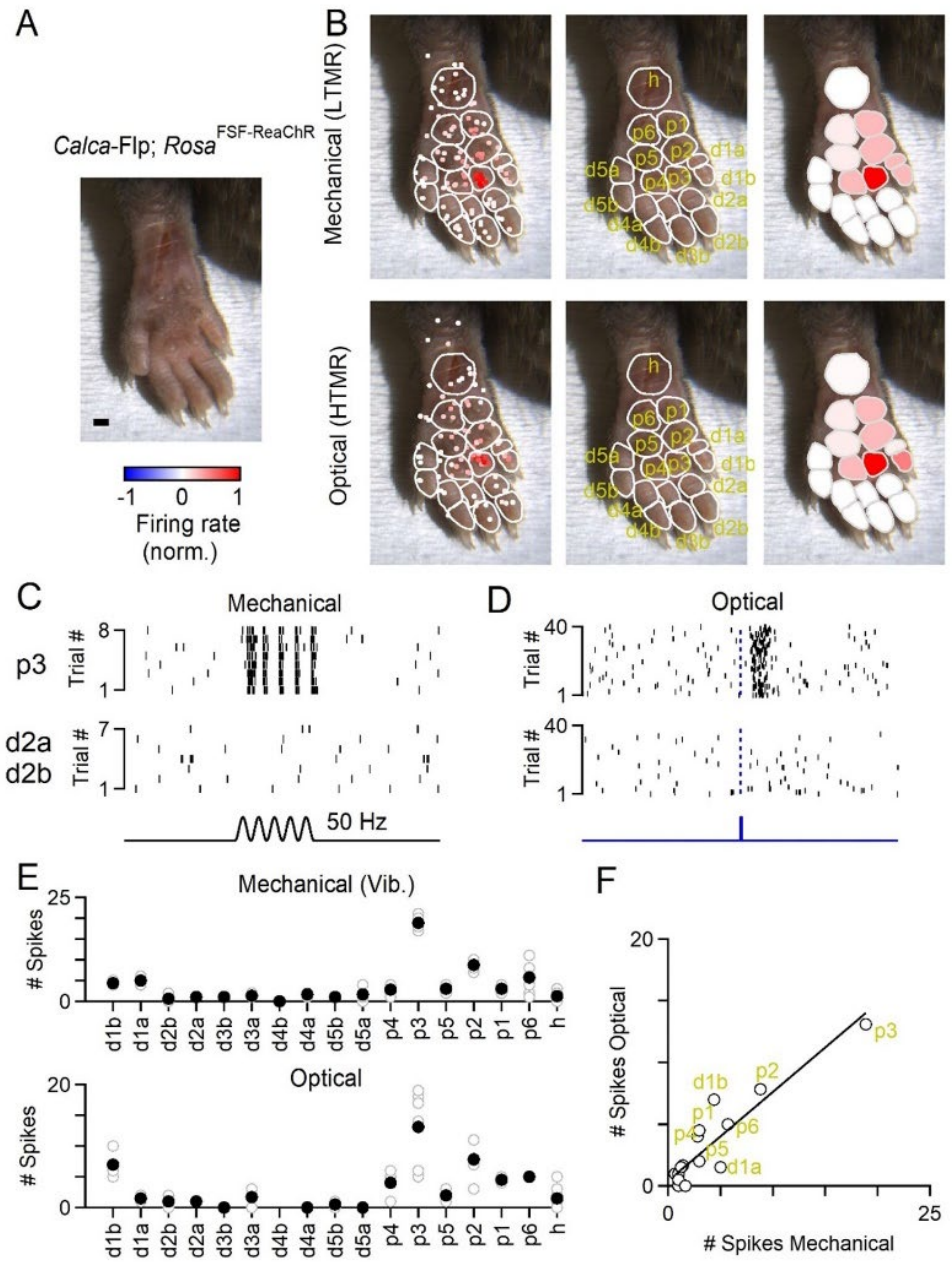

Extended Data Fig. 10: Optical and mechanical receptive field correlation for single units

A. Hindpaw in a *Calca-FlpE*; *Rosa26*$^{FSF\text{-}ReaChR}$ animal. Scalebar is 1 mm.

B. Hindpaw from A with mechanical (top) or optical (bottom) receptive field analysis. Left: Each point corresponds to a single stimulation trial color coded by the units normalized evoked firing rate. Optical responses were normalized to maximally evoked optical response, mechanical responses were normalized to maximally evoked mechanical response. For an individual unit. the paw was divided into regions corresponding to digits (d1-5, proximal a, distal b) pads (p1-6), and broad area of the heel (h). Trials falling outside the border of these subregions were not used for analysis. Middle: Labeled subregions. Right: Evoked firing from all trials within any subunit

were averaged to generate an average evoked firing rate for that subregion. Regions are color coded for average evoked firing rate.

C. Raster of mechanical stimulation trials from pad p3 region (top) and trials from digit d2a and d2b regions (bottom).

D. Raster of optical stimulation trials from p3 region (top) and trials from d2a and 2b regions (bottom). Raw trials included 5 pulses of light delivered at 1 Hz, all delivered pulses are aligned here for presentation. Timescale for C and D are the same.

E. Plot of number of spikes for each subregion for unit shown in B for mechanical (top) and optical (bottom) stimuli. Spike count for optical stimuli included only first 40 ms following the light pulse, corresponding to a putative Aδ evoked response. Counts from individual trials (gray, empty) and average for subregions (black, filled) are shown.

F. Correlation of optically and mechanically evoked firing rate for each subregion of the paw for DCN unit shown in B-D. Each point is a single subregion of the paw, with its y-value corresponding to number of optically-evoked spikes, and x-value corresponding to number of mechanically-evoked spikes. Linear fit is overlaid.

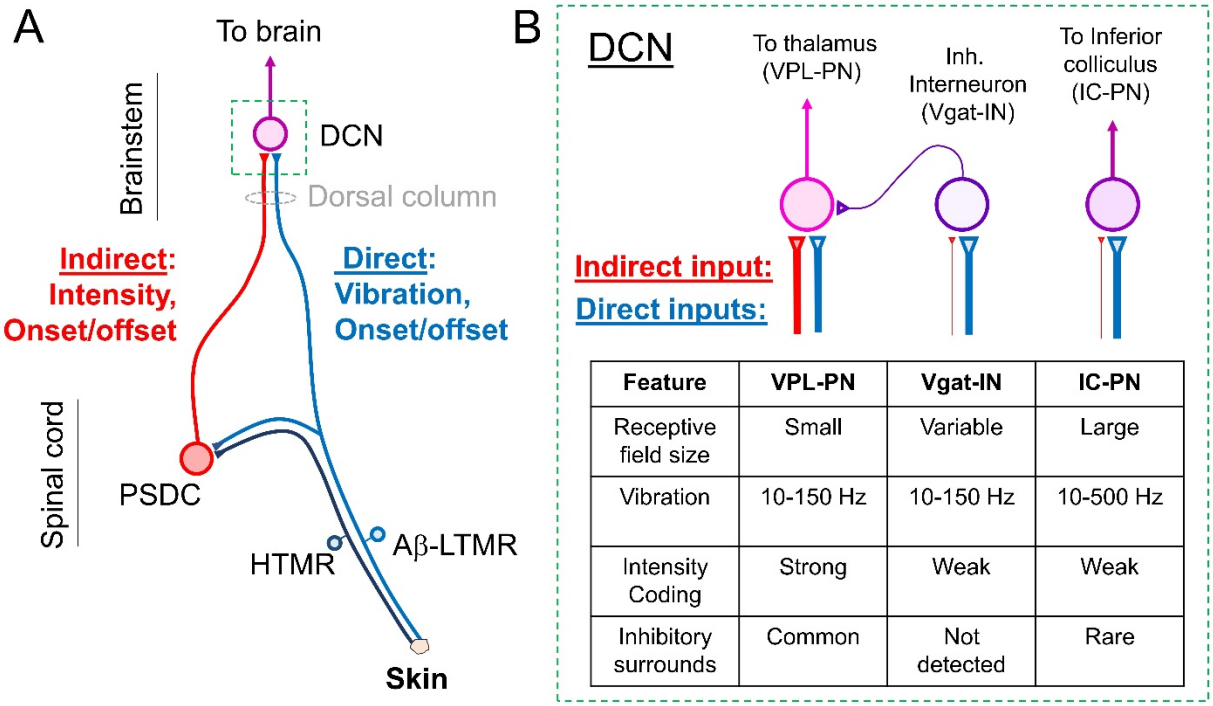

Feature	VPL-PN	Vgat-IN	IC-PN
Receptive field size	Small	Variable	Large
Vibration	10-150 Hz	10-150 Hz	10-500 Hz
Intensity Coding	Strong	Weak	Weak
Inhibitory surrounds	Common	Not detected	Rare

Extended Data Figure 11: A model for sensory representation in the dorsal column system
A. Mechanical stimuli in a small area of skin are detected by LTMRs and HTMRs. LTMRs ascend the dorsal column and synapse onto neurons in the DCN, forming the direct pathway. LTMRs also form collaterals within the spinal cord dorsal horn. PSDCs in the spinal cord dorsal horn receive mechanical information from LTMRs and HTMRs, either directly or through local interneurons. PSDC axons then ascend the dorsal column, forming the indirect pathway. PSDCs of the indirect pathway signal the intensity of sustained stimuli and the onset/offset of stimuli, as well as low-frequency vibratory stimuli. LTMRs of the direct pathway signal rapid movements and high-frequency vibratory stimuli, in addition to the onset/offset of stimulation. These two pathways converge somatotopically such that individual DCN neurons can encode multiple features in a small patch of skin.

B. Different contributions from PSDCs and LTMRs drive distinct response properties in DCN neuron types. *Left*: VPL-PNs have small RF sizes and commonly have inhibitory surrounds driven by DCN Vgat-INs. Direct LTMR input drives phase-locked spiking up to ~150 Hz. VPL-PNs can also commonly encode sustained stimuli at high forces mediated by indirect PSDC input. Thus, VPL-PNs receive prominent direct and indirect input. *Middle:* Local Vgat-INs have varying receptive field sizes and can entrain to vibrations up to 150 Hz. Vgat-INs do not receive prominent indirect input that drives firing in response to sustained stimuli. *Right:* The most common type of IC-PNs (Type 1) have very large receptive field sizes and can entrain to high-frequency vibratory stimuli up to 500 Hz. These high-frequency responses are likely generated exclusively by direct LTMR (Aβ-RA2-LTMR) input. They typically do not receive strong indirect input that can drive firing in response to sustained stimuli. Although Vgat-INs and IC-

PNs do not receive strong HTMR input via PSDCs, they may receive some low-threshold indirect input that could contribute to the onset and offset of stimulation.

894 **Extended Data Table 1: number of experiments**

Figure	Condition/Experiment	N (animals)	n (units)
1D	VPL-PN frequencies	4	6
1E	VPL-PN indentation	10	23
1I	IC-PN frequencies	5	11
1J	IC-PN indentation	5	12
1N	Vgat-IN frequencies	3	10
1O	Vgat-IN indentation	3	12
1P	VPL-PN RF area	10	19
1P	IC-PN RF area	4	11
1P	Vgat-IN RF area	3	12
1Q	VPL-PN inh. Surr.	10	19
1Q	IC-PN inh. Surr.	4	11
1Q	Vgat-IN inh. Surr.	3	12
1R	VPL-PN Spont. Rate	10	23
1R	IC-PN Spont. Rate	5	12
1R	Vgat-IN Spont. Rate	3	12
2C	10 Hz	2	7
2C	50 Hz	3	7
2C	300 Hz	1	5
2D-E	Indentation	1	10
2H	10 Hz	2	9
2H	50 Hz	4	14
2H	300 Hz	2	7
2I-J	Indentation	2	9
2N-Q	Inh. Surr.	6	10
3C	10 Hz NBQX	1	5
3C	50 Hz NBQX	2	12
3C	300 Hz NBQX	1	5
3J-K	Indentation Ctrl.	4	11
3J-K	Indentation NBQX (L3-L5)	4	10
3L	Threshold Ctrl.	15	35
3L	Threshold NBQX (L3-L5)	7	19
3M	Sustained firing Ctrl.	4	11
3M	Sustained firing NBQX (L3-L5)	4	10
4D,G	VPL-PN Calca input	4	14
4M-N	Mech./Optical RFs	2	7
ED1 I-J	VPL-PN CV, jitter	18	45
ED2 C	IC-PN CV, jitter	5	16
ED2 F	IC-PN Type 1 frequencies	5	11
ED2 I	IC-PN Type 2 frequencies	5	9
ED2 J	IC-PN Type 2 frequencies	3	3
ED2 J	IC-PN Type 1	5	16

ED2 J	IC-PN Type 2	5	9
ED2 K	IC-PN Type 3	3	5
ED2 K	VPL-PN Type 1	1	1
ED2 K	VPL-PN Type 2	17	38
ED2 K	VPL-PN Type 3	0	0
ED2 L	VPL-PN Type 2	10	19
ED2 L	IC-PN Type 2	5	7
ED2 M	IC-PN Type 1 inh. Surr.	4	11
ED2 M	IC-PN Type 2 inh. Surr.	5	7
ED2 M	IC-PN Type 3 inh. Surr.	3	3
ED2 M	VPL-PN Type 2 inh. Surr.	10	19
ED3 D	LTMR/PSDC count	4	N/A
ED4 F		4	N/A
ED5 E-F	NBQX T10-T13	2	10
ED6 G	NBQX T10-T13 threshold	3	14
ED6 G	NBQX T10-T13 sustained	2	10
ED7 P-S	VPL indentation (pre/post)	2	31
ED7 T	VPL threshold (pre/post)	4	58
ED7 U	VPL sustained (pre/post)	2	31
ED8 D-F	DCN spont. rate (pre/post)	2	16
ED8 J-L	VPL spont. rate (pre/post)	4	58
ED9 A-B		1	10
ED9 C		10	23
ED9 D		2	17
ED9 E		4	14
ED9 F		1	8

904 **Extended Data Table 2: statistics**

Figure	Experiment	p-value	Statistical test
1P	RF area; VPL/IC-PN	**<0.0001**	Kolmogorov-Smirnov
1P	RF area; VPL-PN/Vgat-IN	0.400	Kolmogorov-Smirnov
1P	RF area; IC-PN/Vgat-IN	**<0.0001**	Kolmogorov-Smirnov
1R	Spont. Rate; VPL-PN/IC-PN	**0.012**	Kolmogorov-Smirnov
1R	Spont. Rate; VPL-PN/Vgat-IN	**<0.0001**	Kolmogorov-Smirnov
1R	Spont. Rate; IC-PN/Vgat-IN	**0.0076**	Kolmogorov-Smirnov
2C	Cdx2; 10 Hz Ctrl/+L	**0.0008**	Paired t-test
2C	Cdx2; 50 Hz Ctrl/+L	**<0.0001**	Paired t-test
2C	Cdx2; 300 Hz Ctrl/+L	**0.0013**	Paired t-test
2H	Adv; 10 Hz Ctrl/+L	0.056	Paired t-test
2H	Adv; 50 Hz Ctrl/+L	**<0.0001**	Paired t-test
2H	Adv; 300 Hz Ctrl/+L	**0.0012**	Paired t-test
2E	Cdx2; Ind. Ctrl/+L	**0.0017**	Paired t-test
2J	Adv; Ind. Ctrl/+L	**0.011**	Paired t-test
2P	Surr. Inh. Ctr/+L	**<0.0001**	Paired t-test
2Q	Rebound Ctr/+L	**0.0015**	Paired t-test
3C	10 Hz Ctrl/NBQX	0.51	Kolmogorov-Smirnov
3C	50 Hz Ctrl/NBQX	0.16	Kolmogorov-Smirnov
3C	300 Hz Ctrl/NBQX	0.51	Kolmogorov-Smirnov
3L	Threshold Ctrl/NBQX	**0.0017**	Kolmogorov-Smirnov
3M	250 mN sus. Z-score Ctrl/NBQX	**0.0009**	Kolmogorov-Smirnov
4N	RF Corr. Mech.-opt./Shuffled	**0.0003**	Kolmogorov-Smirnov
ED1 I	Conduction Velocity VPL/IC-PNs	0.31	Kolmogorov-Smirnov
ED2 L	RF area; VPL/IC-PN type 2	**0.031**	Kolmogorov-Smirnov
ED3 D	PSDCs/LTMRs per segment	**0.017**	Paired t-test
ED5 F	Amplitude Ctrl./NBQX	**<0.0001**	Paired t-test
ED6 G	Threshold Ctrl/NBQX	0.25	Kolmogorov-Smirnov
ED6 G	250 mN sus. Z-score Ctrl/NBQX	0.76	Kolmogorov-Smirnov
ED7 T	Threshold Ctrl/Lesion	**<0.0001**	Kolmogorov-Smirnov
ED7 U	250 mN sus. Z-score Ctrl/NBQX	**<0.0001**	Kolmogorov-Smirnov
ED8 D	Spont. Rate Ctrl/Lesion	0.93	Kolmogorov-Smirnov
ED8 J	Spont. Rate Ctrl/Lesion	**0.0014**	Kolmogorov-Smirnov

905

906

907

908 **METHODS**

909 **Animals**

910 All experimental procedures were approved by the Harvard Medical School Institutional Care
911 and Use Committee and were performed in compliance with the Guide for Animal Care and Use
912 of Laboratory Animals. Animals were housed in a temperature- and humidity-controlled facility
913 and were maintained on a 12:12 hour dark:light cycle. All experiments were performed on adult
914 animals (>5 weeks) of both sexes. The following mouse lines were used: C57Bl/J6; *Calca-FlpE*
915 (ref.[37]); *Calca*^{CreER} (ref.[53]); *Avil*^{FlpO} (ref.[37]); *Avil*^{Cre} (ref.[54]); *Cdx2-Cre* (ref.[47]); *Rosa26*$^{LSL\text{-}Acr1}$
916 (ref.[35]); *Rosa26*$^{FSF\text{-}ReaChR}$ (derived from ref.[55]); *Rosa26*$^{LSL\text{-}FSF\text{-}ReaChR}$ (ref.[55]). Animals were
917 maintained on mixed C57Bl/J6 and 129S1/SvImJ backgrounds. C57Bl/J6 were obtained from
918 Jackson Laboratories. For *Calca*^{CreER}*; Rosa26*$^{LSL\text{-}FSF\text{-}ReaChR}$ mice, 3 mg tamoxifen was
919 administered by intraperitoneal injection at P21.

920 **Juxtacellular recordings**

921 Adult (>5 weeks) animals were anesthetized with urethane (1.5 g/kg) and placed on a heating
922 pad. The head and neck were shaved and local anesthesia (lidocaine HCl, 2%) was administered
923 to the scalp and neck. An incision was made in the skin, and the muscle of the dorsal aspect of
924 the neck was cut and moved aside to expose the brainstem. A headplate was attached to the skull
925 using dental cement and the head was fixed to a custom-built frame. The dura overlying the
926 brainstem was cut and small fragments of the occipital bone were removed. In some cases in
927 which optical access to the DCN was required, small amounts of the posterior vermis of the
928 cerebellum were aspirated to expose the DCN. A glass electrode filled with saline (2-3 MΩ) was
929 put in place 200-300 µm above the gracile nucleus. The area was then flooded with low-melting
930 point agarose. After hardening, the electrode was advanced into the gracile. The electrode was
931 guided to individual units and positioned to maximize the signal of a single unit. Recording
932 quality and unit discrimination was continuously assessed using an audio monitor and online
933 analysis. All recordings in the DCN were made in the hindlimb representation region of the
934 gracile nucleus, and only units with receptive fields in the hindlimb were recorded. Although it
935 has been reported that the gracile in rats, cats and primates is subdivided into 'core' and 'shell'
936 regions, we were unable to detect such organization in the mouse through electrophysiology
937 experiments. Signals from single units were amplified using the 100x AC differential

938 amplification mode of a Multiclamp 700B and sampled at 20 kHz using a Digidata 1550B
939 controlled by Clampex 11 software (Molecular Devices). Signals were collected with an
940 additional 20x gain and 0.3-3 kHz Bessel filter.

941 In some experiments DCN neurons were identified through antidromic activation of their axon in
942 a target region. A craniotomy over the region of interest was performed. The head was leveled
943 and bipolar electrodes (platinum-irridium 250 µm spacing, FHC) was lowered into the
944 contralateral VPL of the thalamus (coordinates: 2 mm posterior to bregma, 2 mm lateral, 3.5 mm
945 deep), or the inferior colliculus (coordinates: head angled 45 degrees, 4 mm posterior to bregma,
946 1 mm lateral, 1.7 mm deep). Single stimuli were applied every 3 sec while searching for units in
947 the DCN. A collision test was performed for all units which could be antidromically activated.
948 Stimuli were triggered from spontaneous spikes, and experiments were only continued for units
949 that passed collision testing. We found that units with reliable and precisely timed antidromic
950 spikes (jitter <1 ms) almost always passed a collision test. Units that failed collision testing had
951 variable timing of activation and much longer latencies. Polysynaptic activation in the DCN was
952 rarely detected by activating the inferior colliculus, and sometimes observed when stimulating
953 the VPL.

954 To record from inhibitory neurons in the DCN, we used optical activation in *Vgat-ChR2* animals.
955 Units were searched while applying 200-300 ms ramps of blue light (2-4 mW/mm^2) from a fiber
956 optic (400 µm diameter, 0.39 NA) placed above the DCN. Light was delivered from a 470 nm
957 LED (M470F3, Thorlabs). Ramps were used because pulses of light were found to generate short
958 latency activation in most units. Most units in the DCN are glutamatergic, and we found that
959 pulsed light drives strong synchronized GABAergic input to primary afferent terminals and
960 stimulates them through the depolarizing action of GABA, thereby driving vesicle release onto
961 excitatory projection neurons. When ramps were used, many units were instead silenced, as
962 expected. Units considered optotagged were those that could be activated during the light ramp.

963 **Optical silencing**

964 For optical silencing of ascending inputs *in vivo*, experiments were prepared as described above
965 except dissection was performed in the dark under red light illumination, as bright white
966 dissection light was capable of activating Acr1. All experiments were performed in animals
967 homozygous for the *Rosa26*$^{LSL\text{-}Acr1}$ allele, as light was unable to fully silence inputs in

968 heterozygous animals. Once the preparation was ready, the electrode was positioned in place
969 above the DCN, along with a 400 µm diameter 0.39 NA fiber 1 mm above the DCN. The area
970 was flooded with low-melting point agarose embedding the fiber and electrode. The electrode
971 was then advanced into the DCN to record from single units.

972 Silencing trials were pseudo-randomly interleaved with control trials. On silencing trials, a 300-
973 400 ms light ramp (0.5 mW/mm^2, 552 nm) was delivered to the surface of the DCN with
974 mechanical stimuli delivered during the last 100-200 ms of the ramp. Light was delivered using a
975 552 nm LED (MINTF4, Thorlabs). We found that silencing became progressively ineffective
976 after 500 ms of light delivery, possibly due to effects of prolonged depolarization of the
977 terminals.

978 **Multielectrode array recordings**

979 Recordings in the thalamus were made in the middle VPL (2 mm bregma, 2 mm lateral, 3.5 mm
980 deep). Animals were headplated, the DCN was exposed as described above, and a craniotomy
981 above the VPL was performed. The dura was removed, and the area was flooded with 2% low-
982 melting agarose dissolved in saline. A 32-channel multi-electrode array (MEA, A1x32-poly2-
983 10mm-50s-177-A32, Neuronexus) was lowered at 5 µm/s into the brain. Once positioned in a
984 region where firing in many units could be evoked by brushing the hindpaw, the MEA was kept
985 in place for 20 minutes to ensure a stable recording. The hindpaw was embedded in playdough
986 for stabilization and the receptive fields of units were quickly assessed using a brush. The
987 mechanical stimulator probe tip was then placed over the region of the hindpaw that could
988 maximally activate the most units. Step indentations of 0-300 mN were applied every 3-6
989 seconds in ascending order and repeated until at least 10 trials per force were obtained.
990 Following stimulation the DCN was lesioned, either by using a 30 gauge needle and striking
991 through the gracile nucleus, or by aspirating the gracile nucleus. Step indentations were then
992 repeated. Throughout the experiment, the waveform of a single unit was monitored closely to
993 assess drift, and any experiment with detectable waveform changes were discarded. In some
994 cases, once the experiment was complete, the MEA was retracted from the brain, coated with DiI
995 (ThermoFisher), and then descended to the same coordinates and allowed to stabilize for 5
996 minutes. Animals were then anesthetized with isoflurane and transcardially perfused with PBS
997 followed by 4% PFA in order to assess the location of the lesion and electrode placement.

998 For lesions of the DC, animals were prepared as described above, and a laminectomy was
999 performed at approximately T12 vertebrae and the dura was removed. A high-density 32-channel
1000 MEA (A1x32-poly3-5mm-25s-177-A32, Neuronexus) was inserted into the gracile nucleus and
1001 allowed to stabilize for 15 minutes. A baseline of 5 minutes of spontaneous firing was collected.
1002 The DC was then lesioned at approximately T12 using a 30 G needle. Brief vibratory stimuli
1003 were applied to the hindlimb throughout the experiment to assess the effectiveness of the lesion.

1004 MEA recordings were made using an Intan headstage, recording controller (Intan Technologies
1005 RHD2132 and Recording Controller) and open-source acquisition software (Intan Technologies
1006 RHX data acquisition software, version 3.0.4). Data was sampled at 20 kHz and bandpassed (0.1
1007 Hz – 7.5 kHz).

1008 ***Ex vivo* recordings**

1009 Intracellular recordings were performed in random DCN neurons ex vivo. The brainstem was
1010 prepared as previously described[13], except DCN neurons were recorded directly from the dorsal
1011 surface of a dissected brainstem. Borosillicate electrodes (2-3 MΩ) filled with internal solution
1012 consisting of in mM: 130 K-gluconate, 3 KCl, 10 HEPES, 0.5 EGTA, 3 MgATP, 0.5 NaGTP, 5
1013 Phosphocreatine-$Tris_2$, 5 Phosphocreatine-Na_2, pH 7.2 with KOH, were visually guided to the
1014 DCN. Experiments were performed in recirculated ACSF containing in mM: 127 NaCl, 2.5 KCl,
1015 1.25 NaH_2PO_4, 1.5 $CaCl_2$, 1 $MgCl_2$, 26 $NaHCO_3$, 25 Glucose. Oxygenated with 95% O2 / 5%
1016 CO2. The preparation was kept at 35°C using an in-line heater. Recordings of random DCN cells
1017 were made using a Multiclamp 700B (Molecular Devices) and acquired using a Digidata 1550B
1018 with Clampex 11 software (Molecular Devices).

1019 **Pharmacology**

1020 For spinal cord silencing experiments, animals were prepared for juxtacellular DCN recordings
1021 as described above. A laminectomy was performed over L3-5 spinal segments, the region of the
1022 spinal cord responsive to hindlimb stimulation. For control experiments, a laminectomy was
1023 performed over T10-T13 spinal segments. The exposed spinal cord and vertebral column was
1024 then flooded with low-melting point agarose. Once hardened, agarose overlying the dorsal horn
1025 was cut away to create a pool and confine drugs to the spinal cord. The dura was removed from
1026 the spinal cord using fine forceps. Prior to drug application, stimuli were applied to the hindpaw

1027 to evoke typical responses to ensure that the spinal cord or dorsal column had not been damaged.
1028 Drugs were then applied to the spinal cord. The non-competitive NMDAR antagonist MK-801
1029 (10 mM, 10 µL, Abcam; dissolved in 90% H_2O, 10% DMSO) was applied to the surface of the
1030 spinal cord and allowed to enter the cord for 3-5 minutes. The surface of the cord was then
1031 irrigated with saline. NBQX (10 mM, 20 µL, Abcam, dissolved in H_2O) was then applied to the
1032 surface of the cord. After 5 minutes, the cord was covered with gelfoam which was allowed to
1033 absorb the NBQX and remained in place for the duration of the experiment, occasionally re-wet
1034 with saline. Drugs were applied sequentially in order to prevent precipitates from drug mixing at
1035 high concentration. Units were then recorded, and animals were sacrificed within 2-3 hours
1036 following drug application.

1037 For controls measuring the efficacy of blockade, a laminectomy was performed over the L4
1038 spinal cord. The vertebral column was held in place by two custom spinal clamps. The dura was
1039 removed using fine forceps or a fine needle and kept moist with saline. A 32-channel MEA was
1040 inserted into medial L4 (A1x32-poly2-10mm-50s-177-A32, Neuronexus). Step indentations (300
1041 mN) were applied at 0.1 Hz, and the MEA was lowered such that the most dorsal channel
1042 detected minimal evoked responses. The location of the dorsal channel was assumed to be near
1043 the surface of the cord. The MEA was then kept in place for 15 minutes. Baseline trials were
1044 collected and then drugs were applied as described above.

1045 **Mechanical and optical stimuli**

1046 We selected for units that were primarily responsive to stimulation of the hindpaw. All
1047 mechanical stimuli were generated by a DC motor with an arm connected to a blunt and
1048 smoothed acrylic probe tip 1 mm in diameter. The motor was driven by a custom-built current
1049 supply controlled by a data acquisition board (Digidata 1550B, Molecular Devices). Step
1050 indentation forces were calibrated using a fine scale. For experiments measuring responses to
1051 various forces, the probe tip was positioned in a resting state on the skin surface and indentations
1052 of incrementally increasing forces were applied every 3-10 seconds. Once the maximal force was
1053 reached, the force was reset to zero and was again incrementally increased. A blunt probe was
1054 used to avoid damaging the skin, and we did not observe visible damage to the skin following
1055 high force stimuli. For experiments measuring responses to vibration, vibratory stimuli were
1056 applied at similar forces (5-15 mN) across frequencies. DCN units that did not respond to

1057 Pacinian-range vibration frequencies also did not respond when vibrations were delivered at
1058 higher forces.

1059 The stimulator was attached to a manipulandum that could be moved by hand and would remain
1060 in position. For receptive field mapping, the probe tip was manually moved over a single
1061 position of the hindlimb where it remained in place. A trial was then initiated to deliver a brief
1062 vibration (50 Hz, 100 ms, 5-15 mN). The experiment was performed under a stereoscope
1063 equipped with a CCD (BlackFly S BFS-U3-04S2C, Flir) that was triggered to capture images for
1064 each trial. This process was repeated until enough trials were acquired (60-100) to generate a
1065 receptive field map of the entire hindpaw. For experiments measuring indentation responses at
1066 various forces, the stimulator was firmly secured to a 0.5" heavy post in order to prevent
1067 relocation or repositioning when applying high forces.

1068 Optical stimulation was performed on the skin or DCN using a 200 µm or 400 µm diameter 0.39
1069 NA fiber coupled to a 554 nm LED (MINTF4, Thorlabs). For skin stimulation, the fiber tip was
1070 held in place with a manipulandum and moved in position manually for each trial, as performed
1071 for mechanical stimulation. Five pulses (2-5 ms duration, 60 mW/mm^2) were delivered to the
1072 skin at 1 Hz for each trial.

1073 **Stereotaxic injections**

1074 Adult animals were anesthetized with isoflurane and placed in a stereotaxic frame. The head was
1075 tilted 30° forward. The hair over the neck and caudal scalp were removed using a clipper and the
1076 skin was sanitized using isopropanol followed by betadine. Local anesthesia (2% lidocaine HCl)
1077 was applied to the area and an incision was made to expose neck muscles. Neck muscles were
1078 separated from the skull to expose the brainstem. A 30-gauge needle was used to cut the dura
1079 overlying the brainstem and expose the DCN. A pipette filled retrograde tracer (Red Retrobeads,
1080 Lumafluor, or cholera toxin subunit B 2 µg/µL, Fisher) and 0.01% fast green was lowered into
1081 the DCN just sufficient to penetrate the surface. Once penetrating the surface, a small volume
1082 (30-50 µL) of retrograde tracer was injected. The pipette was held in place for 20 seconds and
1083 then removed. Care was taken to ensure tracer did not leak from the injection site following
1084 injection, and that tracer labeled with fast green filled the DCN, but did not extend beyond the
1085 nucleus. The pipette was then removed, and overlying muscle and skin was sutured shut.

1086 Animals were administered analgesic (Buprenex SR, 0.1 mg/kg, ZooPharm) and monitored post-
1087 operatively. Following 1-3 days, animals were transcardially perfused for tissue harvest.

1088 **Histology**

1089 Animals were anesthetized with isoflurane and transcardially perfused with PBS followed by 4%
1090 PFA in PBS. Brains were removed and post-fixed in PFA overnight. The spinal cord and DRGs
1091 were dissected free. The isolated spinal cord was mounted in low-melting point agarose and the
1092 thoracic spinal cord 60 µm thick sections were made on a Leica VT1000S vibratome. A subset of
1093 sections underwent immunohistochemistry. Free-floating sections were first permeabilized with
1094 0.1% Triton-X100 in PBS for 30 min at room temperature. Sections were then incubated with
1095 0.1% Triton-X100 and 4% normal goat serum (NGS, Abcam) for 30 min at room temperature.
1096 Primary antibodies were then added (mouse anti-NeuN, 1:1000, MAB377, Millipore) and
1097 incubated overnight at 4°C. Sections were then washed three times with PBS with 0.1% Triton-
1098 X100 and 4% NGS for 10 minutes at room temperature. Secondary antibodies were then applied
1099 (IB4-Alexa 647, 1:300, I32450, ThermoFisher; goat anti-mouse Alexa-488, 1:500, ab150113,
1100 Abcam) for 2 hours at room temperature, and washed with PBS three times for 10 minutes.
1101 Sections were mounted onto glass slides using Fluoromount Aqueous mounting medium
1102 (Sigma). Sections were imaged with a Zeiss LSM 700 confocal microscope using a 20x 0.8 NA
1103 oil immersion objective using Zen software. DRGs were whole-mounted and imaged using a
1104 Zeiss LSM 700 confocal microscope using a 10x 0.45 NA air objective.

1105 PSDCs were counted in Z-stacks (3-4 µm Z-spacing) of 60 µm thick thoracic spinal cord
1106 sections. 10-20 sections were analyzed per animal, and the average number of PSDCs per section
1107 was measured and multiplied by 16.67 to estimate the number PSDCs in one segment (1000 µm)
1108 of spinal cord for that animal. AB-LTMRs were counted in whole-mounted thoracic DRGs and
1109 compared to spinal cords of the same animals. Labeled DRG neurons were counted in Z-stacks
1110 of the entire DRG (5-6 µm Z-spacing). If more than one DRG was analyzed per animal, the
1111 number of counted cells was averaged between the two.

1112 **Analysis**

Juxtacellular recordings in the DCN were analyzed offline using custom written scripts in Matlab (Mathworks). Spikes were detected using an amplitude threshold and recordings in which the unit could not be isolated by amplitude were discarded.

Receptive field maps were generated using custom written scripts in Matlab. An image of the hindpaw from the experiment was used as a template. Images capturing the probe or fiber optic for each trial were cycled through and the location of the probe or fiber tip was manually marked on the template image. The coordinates of each stimulus location and the template image were then combined with electrophysiology data to identify the number of evoked spikes for each stimulus location. Each unit's receptive field map is displayed with points indicating the location of the stimulus and normalized change in firing rate from baseline. The maximal change in firing rate is indicated in text within the image. Maximal firing rate was measured as the number of spikes over the course of the 100 ms vibratory stimulus, or number of spikes within a 20 ms window following optical stimulation. The spontaneous firing rate was measured as the average firing rate prior to mechanical stimulation across trials. In order to measure the receptive field area, a threshold was taken at the half-maximal evoked firing rate. Stimulus locations that evoked the half-maximal firing rate or more were included in the receptive field. The area bound by these points was used as a measure of the receptive field area.

Correlation of optical and receptive fields were performed as shown in Extended Data Figure 9. The optical and mechanical receptive fields were mapped as described above. The paw was then subdivided into segments corresponding to digits and pads. The stimulus trials falling within each segment were averaged to obtain and average evoked firing rate for each segment. The optically-evoked firing rate for each segment was plotted against its mechanically evoked firing rate. A linear fit was performed and the Pearsons correlation coefficient (R^2) was used as a measure of receptive field correlation. As a control, similar analysis was performed but optical and mechanical receptive fields were shuffled between units.

Spike sorting (MEAs)

MEA recordings underwent initial analysis using Kilosort 2.0 (ref. [56]). Prior to analysis, baseline and lesions trials were interleaved in order to prevent artifactual drift corrections by Kilosort. Drift monitoring was performed during acquisition and experiments with detectable changes in spike waveforms were discarded. Default detection settings were used for analysis, except

template amplitude thresholds were set to [5 2]. Clustered were manually curated using Phy[57] by examining spike waveforms and autocorrelations in order to identify putative single units. As receptive fields were not mapped for MEA experiments, units underwent selection for inclusion. Units that had low thresholds at baseline (<10 mN), or units that had mechanically-evoked firing that was unaffected by lesioning the DCN were included. Units that had high-thresholds (>10 mN) at baseline and became mechanically insensitive following DCN lesion were not included for analysis because the stimulus may have been off the center of the receptive field.

Z-scores were computed by measuring the average baseline firing rate within a 0.5-1 s window prior to stimulation. For optical silencing, pharmacology and lesion experiments in which the same units were monitored before and after manipulation, Z-scores in experimental conditions were computed from the mean and standard deviations of baseline trials.

Statistical analyses

Statistical analyses were performed with significance threshold set at $p < 0.05$. All summary data is presented as mean ±SEM unless otherwise noted. All t-tests were two-sided.

Data availability

Data generated during this study will be included in this published article (and its supplementary information files) upon acceptance of the manuscript.

Code availability

Custom scripts used in this study will be posted to Github upon acceptance of the manuscript.

ACKNOWLEDGEMENTS

We thank Christopher Harvey, Chinfei Chen, Wade Regehr, Celine Santiago, Alan Emanuel, Genelle Rankin, Andrew Shuster, Anda Chirila, Rosa Martinez-Garcia, Dawei Zhang, and Jessica Barowski for comments on the manuscript. This work was supported by a Mahoney Postdoctoral Fellowship (JT), a Gordon Postdoctoral Fellowship (JT), NIH grant NS097344 (DDG), The Hock E. Tan and Lisa Yang Center for Autism Research at Harvard University (DDG), and the Edward R. and Anne G. Lefler Center for Neurodegenerative Disorders (DDG). DDG is an investigator of the Howard Hughes Medical Institute. This article is subject to HHMI's Open Access to Publications policy. HHMI lab heads have previously granted a nonexclusive CC BY 4.0 license to the public and a sublicensable license to HHMI in their research articles. Pursuant to those licenses, the author-accepted manuscript of this article can be made freely available under a CC BY 4.0 license immediately upon publication.

AUTHOR CONTRIBUTIONS

JT, BPL, and DDG conceived the project. JT performed all experiments except data shown in Extended Data Fig. 3. JT performed all analysis. BPL performed pilot experiments not presented, and anatomical experiments shown in Extended Data Fig. 3. JT and DDG wrote the paper with input from BPL.

COMPETING INTERESTS

The authors declare no competing interests.

REFERENCES

1. Nathan, P. W., Smith, M. C. & Cook, A. W. Sensory effects in man of lesions of the posterior columns and some other pathways. *Brain* **109**, 1003–1041 (1986).

2. Abraira, V. E. & Ginty, D. D. The sensory neurons of touch. *Neuron* **79**, 618–639 (2013).

3. Mountcastle, V. B. *The sensory hand: neural mechanisms of somatic sensation*. (Harvard University Press, 2005).

4. Saal, H. P. & Bensmaia, S. J. Touch is a team effort: Interplay of submodalities in cutaneous sensibility. *Trends in Neurosciences* **37**, 689–697 (2014).

5. Brown, A. G. & Fyffe, R. E. W. Form and function of dorsal horn neurones with axons ascending the dorsal columns in cat. *J. Physiol* **321**, 31–47 (1981).

6. Madsen, A. M. Postsynaptic Dorsal Column Pathway of the Rat. I. Anatomical Studies. *Journal of Neurophysiology* **51**, 260–275 (1984).

7. Cliffer, K. D., Willis, W. D. & Institute, M. B. Distribution of the Postsynaptic Dorsal Column Projection in the Cuneate Nucleus of Monkeys. *Journal of Comparative Neurology* **345**, 93 (1994).

8. Ochoa, J. & Torebjork, E. Sensations evoked by intraneural microstimulation of single mechanoreceptor units innervating the human hand. *The Journal of Physiology* **342**, 633–654 (1983).

9. Weber, A. I. *et al.* Spatial and temporal codes mediate the tactile perception of natural textures. *Proc Natl Acad Sci U S A* **110**, 17107–17112 (2013).

10. Handler, A. & Ginty, D. D. The mechanosensory neurons of touch and their mechanisms of activation. *Nature Reviews Neuroscience* **22**, 521–537 (2021).

11. Johnson, K. O. & Hsiao, S. S. Neural mechanisms of tactual form and texture perception. *Annu Rev Neurosci* **15**, 227–250 (1992).

12. Blomqvist, A., Flink, R., Bowsher, D., Griph, S. & Westman, J. Tectal and thalamic projections of dorsal column and lateral cervical nuclei: a quantitative study in the cat. *Brain Research* **141**, 335–341 (1978).

13. Lehnert, B. P. *et al.* Mechanoreceptor synapses in the brainstem shape the central representation of touch. *Cell* **184**, 5608-5621.e18 (2021).

14. Berkley, K. J., Bwdell, R. J., Blomqvist, A. & Bull, M. Output Systems of the Dorsal Column Nuclei in the Cat. *Brain Research Reviews, ll* 199–225 (1986).

15. Molinari, H. H., Dostrovsky, J. 0 & Moiinari, H. H. Functional properties of neurons in the cat gracile nucleus that project to the dorsal accessory olive. *Exp Brain Res* **69**, (1987).

16. Berkley, K. J. & Hand, P. J. Efferent projections of the gracile nucleus in the cat. *Brain Research* **153**, 263–283 (1978).

17. Suresh, A. K. *et al.* Sensory computations in the cuneate nucleus of macaques. *Proceedings of the National Academy of Sciences* **118**, 2115772118 (2021).

1230 18. Gordon, G. & Jukes, M. G. M. Dual organization of the exteroceptive components of the cat's
1231 gracile nucleus. *The Journal of Physiology* **173**, 263–290 (1964).

1232 19. Jörntell, H. *et al.* Segregation of tactile input features in neurons of the cuneate nucleus. *Neuron*
1233 **83**, 1444–1452 (2014).

1234 20. Cliffer, K. D., Hasegawa, T. & Willis, W. D. Responses of Neurons in the Gracile Nucleus of Cats
1235 to Innocuous and Noxious Stimuli: Basic Characterization and Antidromic Activation From the
1236 Thalamus. *Journal of Neurophysiology* **68**, (1992).

1237 21. Khalsa, P. S. Encoding of Compressive Stress During Indentation by Slowly Adapting Type I
1238 Mechanoreceptors in Rat Hairy Skin. *Journal of Neurophysiology* **87**, 1686–1693 (2002).

1239 22. Emanuel, A. J., Lehnert, B. P., Panzeri, S., Harvey, C. D. & Ginty, D. D. Cortical responses to
1240 touch reflect subcortical integration of LTMR signals. *Nature* **600**, 680–685 (2021).

1241 23. Koltzenburg, M., Stucky, C. L. & Lewin, G. R. Receptive Properties of Mouse Sensory Neurons
1242 Innervating Hairy Skin. *Journal of Neurophysiology* **78**, 1841–1850 (1997).

1243 24. Neubarth, N. L. *et al.* Meissner corpuscles and their spatially intermingled afferents underlie
1244 gentle touch perception. *Science (1979)* **368**, (2020).

1245 25. Rustioni, A. & Kaufman, A. B. *Identification of Cells of Origin of Non-Primary Afferents to the*
1246 *Dorsal Column Nudei of the Cat*. *Brain Res* vol. 27 (1977).

1247 26. Brown, A. G. & Fyffe, R. E. W. Form and function of dorsal horn neurones with axons ascending
1248 the dorsal columns in cat. *The Journal of Physiology* **321**, 31–47 (1981).

1249 27. Noble, R., Riddellt, J. S. & Riddell, J. S. Cutaneous excitatory and inhibitory input to neurones of
1250 the postsynaptic dorsal column system in the cat. *Journal of Physiology* **396**, 497–513 (1988).

1251 28. Cliffer, K. D., Willis, W. D. & Institute, M. B. Distribution of the Postsynaptic Dorsal Column
1252 Projection in the Cuneate Nucleus of Monkeys. *Journal of Comparative Neurology* **345**, 93
1253 (1994).

1254 29. Paixão, S. *et al.* Identification of Spinal Neurons Contributing to the Dorsal Column Projection
1255 Mediating Fine Touch and Corrective Motor Movements. *Neuron* **104**, 749-764.e6 (2019).

1256 30. Rustioni, A. Non-primary afferents to the nucleus gracilis from the lumbar cord of the cat. *Brain*
1257 *Research* 81–95 (1973).

1258 31. Maxwell, D. J., Koerber, H. R. & Bannatynet, B. A. Light and electron microscopy of contacts
1259 between primary afferent fibres and neurones with axons ascending the dorsal columns of the
1260 feline spinal cord. *Neuroscience* **16**, 375–394 (1985).

1261 32. Abraira, V. E. & Ginty, D. D. The sensory neurons of touch. *Neuron* **79**, 618–639 (2013).

1262 33. Abraira, V. E. *et al.* The Cellular and Synaptic Architecture of the Mechanosensory Dorsal Horn.
1263 *Cell* **168**, 295-310.e19 (2017).

1264 34. Madsen, A. M. Postsynaptic Dorsal Column Pathway of the Rat. I. Anatomical Studies. *Journal of*
1265 *Neurophysiology* **51**, (1984).

1266 35. Li, N. *et al.* Spatiotemporal constraints on optogenetic inactivation in cortical circuits. *Elife* **8**,
1267 (2019).

1268 36. Bai, L. *et al.* Genetic Identification of an Expansive Mechanoreceptor Sensitive to Skin Stroking.
1269 *Cell* **163**, 1783–1795 (2015).

1270 37. Choi, S. *et al.* Parallel ascending spinal pathways for affective touch and pain. *Nature* **587**, 258–
1271 263 (2020).

1272 38. Hooks, B. M., Lin, J. Y., Guo, C. & Svoboda, K. Dual-channel circuit mapping reveals
1273 sensorimotor convergence in the primary motor cortex. *Journal of Neuroscience* **35**, 4418–4426
1274 (2015).

1275 39. Mccarthy, P. W. & Lawson, S. N. Cell type and conduction velocity of rat primary sensory
1276 neurons with calcitonin gene-related peptide-like immunoreactivity. *Neuroscience* **34**, 623–632
1277 (1990).

1278 40. Hoheisel, U., Mense, S. & Scherotzke, R. Anatomy and Calcitonin gene-related peptide-
1279 immunoreactivity in functionally identified primary afferent neurones in the rat. *Anat Embryol*
1280 **189**, 41–50 (1994).

1281 41. Arcourt, A. *et al.* Touch Receptor-Derived Sensory Information Alleviates Acute Pain Signaling
1282 and Fine-Tunes Nociceptive Reflex Coordination. *Neuron* **93**, 179–193 (2017).

1283 42. Ghitani, N. *et al.* Specialized Mechanosensory Nociceptors Mediating Rapid Responses to Hair
1284 Pull. *Neuron* **95**, 944-954.e4 (2017).

1285 43. Hooks, B. M. & Chen, C. Distinct Roles for Spontaneous and Visual Activity in Remodeling of
1286 the Retinogeniculate Synapse. *Neuron* **52**, 281–291 (2006).

1287 44. Huberman, A. D., Feller, M. B. & Chapman, B. Mechanisms underlying development of visual
1288 maps and receptive fields. *Annual Review of Neuroscience* vol. 31 479–509 (2008).

1289 45. Dykes, R. W. & Craig, A. D. Control of Size and Excitability of Mechanosensory Receptive
1290 Fieldsin Dorsal Column Nuclei by Homolateral Dorsal Horn Neurons. *Journal of Neurophysiology*
1291 **80**, 120–129 (1998).

1292 46. Noble, R. & Riddellt, J. S. Descending influences on the cutaneous receptive fields of postsynaptic
1293 dorsal column neurons in the cat. *Journal of Physiology* **408**, 167–183 (1989).

1294 47. Coutaud, B. & Pilon, N. Characterization of a novel transgenic mouse line expressing Cre
1295 recombinase under the control of the Cdx2 neural specific enhancer. *Genesis* **51**, 777–784 (2013).

1296 48. Versteeg, C., Rosenow, J. M., Bensmaia, S. J. & Miller, L. E. Encoding of limb state by single
1297 neurons in the cuneate nucleus of awake monkeys. *Journal of Neurophysiology* **126**, 693–706
1298 (2021).

1299 49. Ferrington, D. G., Horniblow, S. & Rowe, M. J. Temporal patterning in the responses of gracile
1300 and cuneate neurones in the cat to cutaneous vibration. *The Journal of Physiology* **386**, 277–291
1301 (1987).

1302 50. Gordon, G. & Jukes, M. G. M. Descending influences on the exteroceptive organizations of the
1303 cat's gracile nucleus. *The Journal of Physiology* **173**, 291–319 (1964).

51. Flavell, C. R., Cerminara, N. L., Apps, R. & Lumb, B. M. Spino-olivary projections in the rat are anatomically separate from postsynaptic dorsal column projections. *Journal of Comparative Neurology* **522**, 2179–2190 (2014).

52. Francis, J. T., Xu, S. & Chapin, J. K. Proprioceptive and cutaneous representations in the rat ventral posterolateral thalamus. *Journal of Neurophysiology* **99**, 2291–2304 (2008).

53. Song, H. *et al.* Functional characterization of pulmonary neuroendocrine cells in lung development, injury,and tumorigenesis. *Proc Natl Acad Sci U S A* **109**, 17531–17536 (2012).

54. Zhou, X. *et al.* Deletion of PIK3C3/Vps34 in sensory neurons causes rapid neurodegeneration by disrupting the endosomal but not the autophagic pathway. *Proc Natl Acad Sci U S A* **107**, 9424–9429 (2010).

55. Hooks, B. M., Lin, J. Y., Guo, C. & Svoboda, K. Dual-channel circuit mapping reveals sensorimotor convergence in the primary motor cortex. *Journal of Neuroscience* **35**, 4418–4426 (2015).

56. Pachitariu, M., Steinmetz, N., Kadir, S., Carandini, M. & Harris, K. D. Kilosort: realtime spike-sorting for extracellular electrophysiology with hundreds of channels. *BioRxiv* **061481**, (2016).

57. Rossant, C. *et al.* Spike sorting for large, dense electrode arrays. *Nature Neuroscience* **19**, 634–641 (2016).